

Time-average and time-dependent parts of core flow

Hagay Amit* and Peter Olson

April 11, 2005

Department of Earth and Planetary Sciences, Johns Hopkins University, Baltimore, MD 21218, USA

* Corresponding author.

E-mail address: hagay@jhu.edu (H. Amit).

Abstract

We infer fluid motions below the core-mantle boundary by inverting geomagnetic secular variation data over a 100 years, assuming helical-geostrophic flow. We obtain snapshot images of core flow at 5 year intervals, which we combine to give time-average and time-dependent parts of the motion over this time interval. The most prominent time-average flow structure is a large anti-cyclonic vortex in the southern hemisphere beneath the Atlantic and Indian Oceans. The time-average zonal core flow outside the inner core tangent cylinder is significantly westward in the southern hemisphere but nearly zero in the northern hemisphere. Westward polar vortices occur inside the tangent cylinder in both hemispheres, particularly in the north. In terms of mantle versus core origins, mantle driving appears to be responsible for the mid-latitude asymmetry in the zonal core flow, whereas core driving appears to be responsible for the flow at high latitudes. We also compare changes in the core's angular momentum calculated from our time-dependent core flow with changes in the mantle's angular momentum derived from decade-scale length-of-day variations and find adequate agreement. A fit of our time-dependent core flow to a torsional oscillations model yields dominant periods of 88 and 48 years.

Keywords: core flow, geomagnetic secular variation, thermal wind, mantle tomography, geodynamo, length-of-day variations, torsional oscillations.

1 Introduction

The Earth's magnetic field is generated by fluid flow in the Earth's metallic liquid outer core. This process, the geodynamo, has been studied using various approaches, including inversions of the geomagnetic secular variation, self-consistent numerical dynamos, lab experiments, paleomagnetic observations, and core thermal history. In this paper we use the historical geomagnetic secular variation to image the core flow over a century of time. We separate the time-average and time-dependent parts of the core flow derived this way. We compare the time-average flow with models of core flow driven by lateral density gradients originating in the core and in the mantle. Then we compare the time-dependent part of the flow with observed length-of-day variations, and fit these fluctuations to a model of torsional oscillations in the outer core.

The outline of the paper is as follows. In section 2 we describe our method of finding core flow just below the core-mantle boundary from geomagnetic secular variation data. In section 3 we present the results of our inversions using historical secular variation data. In section 4 we apply a thermal wind interpretation to the time-average core flow using mantle tomography and numerical dynamos. In section 5 we use observations of length-of-day variations to test the time-dependent part of our solutions, and we fit a torsional oscillations model to this time-dependency. Our main findings are summarized in section 6.

2 Core flow inversion

The geomagnetic secular variation has been used to map fluid motion in the outer core, providing images of the geodynamo just below its outer surface. Early analysis of the secular variation inferred that the main core flow is uniform $0.2^\circ/\text{yr}$ westward zonal drift (Bullard et al., 1950). More recent analysis of secular variation using the magnetic induction equation in the perfect conducting, frozen-flux limit (Roberts and Scott, 1965) have shown that this simple model is inadequate. It is now known that the zonal core flow varies with latitude and is time-dependent. In addition, core flow includes significant north-south toroidal and poloidal components (Gire et al., 1986; Voorhies, 1986; Jault et al., 1988; Bloxham, 1989; Gire and

LeMouél, 1990; Bloxham and Jackson, 1991; Jackson and Bloxham, 1991; Jackson et al., 1993; Jackson, 1997; Pais and Hulot, 2000; Hulot et al., 2002; Amit and Olson, 2004).

Separate interpretations have been applied to the time-average and the time-dependent parts of the flow. The time-average part of the core flow has been proposed to be a result of mantle heterogeneity (thermal, compositional or topographic) affecting core dynamics (Glatzmaier et al., 1999; Olson and Christensen, 2002; Christensen and Olson, 2003). The time-dependent part has been linked to angular momentum exchange between the core and the mantle and length-of-day variations (Jault et al., 1988; Jackson et al., 1993). The time-dependent core flow has been modeled as torsional oscillations in the outer core (Zatman and Bloxham, 1997; Bloxham et al., 2002).

We wish to stress the conceptual difference between time-average core flow as derived in this paper and previous steady core flow models. We invert for the core flow at each separate epoch, and then calculate the time-average of the resulting flows. This procedure differs from often-used inversion methods which incorporate steady flow (Gubbins, 1982; Voorhies, 1986; Bloxham, 1992) or a steady flow in an azimuthally drifting reference frame (Voorhies and Backus, 1985; Holme and Whaler, 2001) as *a-priori* constraints.

2.1 Inversion method

Fluid motion just below the core-mantle boundary can be inferred from geomagnetic secular variation by assuming the magnetic field acts like a tracer in the fluid. Like previous studies of core flow, we assume frozen magnetic flux, in which the diffusion of magnetic field is neglected in comparison with the advection of magnetic field by the flow (Roberts and Scott, 1965). The frozen flux hypothesis is assumed valid because the magnetic diffusion time-scale, $\tau_\lambda = L^2/\lambda \sim 30,000$ yr, is much longer than the advection time-scale, $\tau_u = L/U \sim 60$ yr, where L , U and λ are the typical length-scale, velocity and magnetic diffusivity for the Earth's core.

The radial component of the frozen flux magnetic induction equation just below the core-

mantle boundary is

$$\frac{\partial B_r}{\partial t} + \vec{u}_h \cdot \nabla B_r + B_r \nabla_h \cdot \vec{u}_h = 0 \quad (1)$$

where B_r is the radial component of the magnetic field, t is time and \vec{u}_h is the fluid velocity tangent to the spherical core-mantle boundary. Maps of B_r and its time derivative $\partial B_r / \partial t$ at the core-mantle boundary allow for inversion of the tangential fluid velocity \vec{u}_h using (1).

The tangential velocity can be decomposed into a toroidal (non-divergent) component expressed in terms of a streamfunction Ψ and a poloidal (divergent) component expressed in terms of a scalar potential Φ as follows:

$$\vec{u}_h = \vec{u}_{tor} + \vec{u}_{pol} = \nabla \times \Psi \hat{r} + \nabla_h \Phi \quad (2)$$

where \hat{r} is a unit radial vector and $\nabla_h = \nabla - \partial / \partial r$ in a spherical coordinate system (r, θ, ϕ) . Substitution of (2) into (1) gives

$$\frac{\partial B_r}{\partial t} + \frac{1}{R^2 \sin \theta} \left(\frac{\partial \Psi}{\partial \phi} \frac{\partial B_r}{\partial \theta} - \frac{\partial \Psi}{\partial \theta} \frac{\partial B_r}{\partial \phi} \right) + \frac{1}{R^2} \left(\frac{\partial \Phi}{\partial \theta} \frac{\partial B_r}{\partial \theta} + \frac{1}{\sin^2 \theta} \frac{\partial \Phi}{\partial \phi} \frac{\partial B_r}{\partial \phi} \right) + B_r \nabla_h^2 \Phi = 0 \quad (3)$$

where $\nabla_h^2 = \nabla^2 - \frac{1}{r^2} \frac{\partial}{\partial r} (r^2 \frac{\partial}{\partial r})$ and R is the core radius.

Amit and Olson (2004) proposed an expression for the tangential divergence of velocity that incorporates the previously-used tangential geostrophy assumption (LeMouél, 1984; Gire and LeMouél, 1990; Jackson, 1997; Hulot et al., 2002) and a helical flow assumption,

$$\nabla_h \cdot \vec{u}_h = \mp k \zeta + \frac{\tan \theta}{R} u_\theta \quad (4)$$

The first term on the right hand side of (4) is helical flow. It assumes that the tangential divergence is correlated with the radial vorticity ζ , the minus sign for the northern hemisphere and the plus sign for the southern hemisphere. The second term on the right hand side of (4) is tangential geostrophy. Substitution of (2) into (4) yields

$$\nabla_h^2 \Phi = \mp k \nabla_h^2 \Psi + \frac{\tan \theta}{R^2} \left(\frac{1}{\sin \theta} \frac{\partial \Psi}{\partial \phi} + \frac{\partial \Phi}{\partial \theta} \right) \quad (5)$$

The non-dimensional parameter k is unknown in the core. Simple analytical models of rotational flows and results from numerical dynamos suggest that $0.5 > k > 0.05$ (Amit and Olson, 2004). Here we use $k = 0.1$, as in the main case of Amit and Olson (2004).

We solve (3) and (5) simultaneously in an iterative way to obtain the potentials Ψ and Φ over the core-mantle boundary. We use a second order, central finite difference method on a regular $2.5^\circ \times 2.5^\circ$ spherical grid with radius R . Equation (5) is singular at the equator, and special treatment is required there. First, we calculate the θ -derivatives of Ψ at the equator by assuming that the equator is a streamline, and the θ -derivatives of Φ at the equator by assuming that the equator is a mirror for Φ . Second, we replace the $\tan \theta$ term in (5) by $-2 \sin(2(\theta - \pi/2)) \cdot \exp(-(\theta - \pi/2)^2)$, which is finite at the equator. These approximations result in a globally balanced upwelling distribution, as opposed to concentrated upwelling features at the equatorial region found in many previous core flow solutions. This treatment corresponds to a non-geostrophic belt near the equator which is plausible because the Coriolis force vanishes there. Previous studies have postulated the existence of such a belt and discussed its possible width and geometry (Backus and LeMouël, 1986; Chulliat and Hulot, 2000; Pais et al., 2004).

2.2 Limitations of core flow inversions

Core flow inversions from geomagnetic secular variation data suffer from several limitations, leading to uncertainties in inferred core flows. First, the secular variation data is truncated at spherical harmonic degree 12 – 14 to remove the effect of crustal magnetization. This truncation might remove a significant core signal, and its influence on the inverted flows is unknown. Second, most studies assume frozen flux, so the unmodeled effects of magnetic diffusion are sources of errors in inverted flows. Third, the physical assumption for the tangential divergence of the core flow is rather ad-hoc. A variety of physical assumptions have been used in the past, such as pure toroidal flow (Whaler, 1980), steady flow (Voorhies, 1986) and tangential geostrophy (LeMouël, 1984). Those assumptions reduce but do not remove non-uniqueness from the inverse problem. This non-uniqueness is of great concern; there is some “invisible” component to the flow which does not generate secular variation of its own (Backus, 1968; Backus and LeMouël, 1986). In tangential geostrophy the non-uniqueness is confined to ambiguous patches and is therefore more restricted than in pure toroidal flow (Chulliat and Hulot, 2000), but still the problem remains. Core flow models which assumed steady flow are advantageous for their simplicity and were found compatible with the gross secular variation, but

could not resolve adequately the fine scale or abrupt secular variation (Bloxxham, 1992; Holme and Whaler, 2001). Finally, different numerical techniques and regularization conditions may affect the resulted core flows as well. Cautious interpretation of the results is necessary in view of these uncertainties. Even so, the remaining uncertainties raise the question whether the inverted core flows give an accurate picture of the actual core flow, in terms of pattern and magnitude. The present study is subject to all of the above limitations, except one. In our method non-uniqueness is removed from the inverse problem by adding helical flow (Amit and Olson, 2004).

3 Core flows between 1895-1985

We solve (3) and (5) for the core flow using the time-dependent model of Bloxxham and Jackson (1992) for the radial component of the magnetic field on the core-mantle boundary $B_r(\theta, \phi, t)$ truncated at spherical harmonic degree 14. This field model was constructed by fitting the magnetic observatory annual means and Magsat satellite data using spherical harmonics for spatial representation and cubic B-splines for the temporal representation. We concentrate on the time interval 1890-1990. We compute the secular variation as the central time difference between two epochs 10 years apart. Accordingly, our core flows correspond to 5-years intervals between 1895-1985. Fig. 1 shows examples of the geomagnetic data used in this study.

Fig. 2 shows core flows for epochs 1900, 1925, 1950, and 1975. Three flow structures are common to all of these snapshots. First, a large anti-cyclonic vortex at mid and high latitudes of the southern hemisphere is centered beneath the southern Atlantic Ocean. This structure drifts slowly westward with time. In 1900 it was centered near $[50E, 45S]$ (Fig. 2a) whereas in 1975 its center moved to near $[15E, 55S]$ (Fig. 2d). In 1925, 1950, and 1975 this structure covers most of the southern hemisphere, extending between $170W$ and $130E$ and from near $20S$ to the South Pole. Second, an intense jet is located beneath the Atlantic southern hemisphere, and forms the northern limb of the vortex. During most epochs its peak intensity is found beneath Southern Africa and beneath mid-latitudes of the Indian and Atlantic Oceans (Fig. 2). Third, an anti-cyclonic vortex is centered beneath the east coast of North America (Fig. 2). Its position, shape and intensity vary with time. A cyclonic vortex beneath Euro-Asia is

also evident in Figs. 2a, 2b, and 2c, but it appears even more time-dependent than the vortex beneath North America.

Table 1 summarizes the magnitudes of the core flows in the snapshot images. Rms core velocities range between 11.4 – 14.8 km/yr, with peak velocities ranging between 82.6 – 153.9 km/yr. For typical length-scale of $L = 1000$ km and magnetic diffusivity of $\lambda = 1$ m²/s, these rms velocities correspond to a magnetic Reynolds number range of $Rm = 360 - 470$. Toroidal motions dominate over poloidal motions. For example, the ratio of rms zonal azimuthal transport (due to toroidal motions only) to rms zonal meridional transport (due to poloidal motions only) varies between 5.4 and 13.4 over the study period.

Some of the core flow structures in Fig. 2 have been seen in previous studies. The westward jet below southern Africa is present in several previous core flow maps (Bloxham, 1989; Gire and LeMouél, 1990). The large southern hemisphere vortex was found by Jackson et al. (1993). Some important differences between our core flows and previous studies are worth noting. First, our core flows contain a significant amount of field-aligned motion, i.e. motion parallel to B_r -contours. This flow component does not generate secular variation by toroidal advection, but it is coupled to upwelling and downwelling which disperse and concentrate the magnetic field respectively. The rms ratio between the field-aligned component of the flow to the component of the flow perpendicular to B_r contours is ~ 1.2 . Field-aligned flow was previously suggested from numerical dynamos and magnetic field observations. Olson et al. (1999) found that vortices coincide with intense magnetic flux bundles in 3D self-consistent numerical dynamos, i.e. the flow there is field-aligned. Jackson (2003) noticed the existence of matching pairs of intense magnetic flux with opposite signs on different sides of the equator in magnetic field models obtained from Magsat (1980) and Oersted (2000) satellites. He postulated that those pairs are evidence for columnar flow. According to this interpretation, that flow at the regions of those flux bundles is parallel to B_r -contours. Second, the relationship between toroidal and poloidal motions is different in our solutions compared to previous solutions. In places where tangential geostrophy dominates, upwelling coincides with equatorward motion and downwelling coincides with poleward motion. However, in places where helical flow dominates, upwelling coincides with anticyclonic motion and downwelling coincides with cyclonic motion.

4 Time-average core flow

Fig. 3a shows the time-average core flow map for the period 1895-1985 constructed by averaging the potentials Ψ and Φ over the 19 epochs. The main features in the time-average core flow include the same structures noted in the snapshots: a large anti-cyclonic vortex centered near $[20E, 60S]$ in the southern hemisphere, an anti-cyclonic vortex below North America centered near $[90W, 40N]$, and a westward jet below the mid-latitudes of the southern hemisphere with peak intensity below Madagascar. Note that the Atlantic hemisphere is more active overall than the Pacific hemisphere. The rms and maximum absolute velocities of the time-average core flow are smaller than the velocities at individual snapshots (Table 1), indicating that the time-average core flow has larger-scale and lower kinetic energy than individual snapshots.

Fig. 3b shows the time-average zonal angular velocity profile for the time interval 1895-1985. Fig. 4 shows the zonal azimuthal velocity (a), meridional velocity (b), and tangential divergence (c) for the same time, and the non-dipolar magnetic flux intensity of the time-average magnetic field between 1895-1985 (d). The net divergence in the time-average flow as well as in the individual snapshot flows is practically zero within the discretization error. As seen in Fig. 3b, the zonal time-average angular velocity is noticeably asymmetric with respect to the equator. At some latitudes it exceeds the traditional 0.2 $^{\circ}/\text{yr}$ westward drift estimate, particularly in the southern hemisphere, although its rms value is only 0.1 $^{\circ}/\text{yr}$. In the northern hemisphere the time-average zonal core flow is nearly zero. The largest zonal angular velocities in Fig. 3b are in westward polar vortices. The northern polar vortex reaches an angular velocity of 1.4 $^{\circ}/\text{yr}$, more than 10 times than the maximal zonal angular velocity at low and mid-latitudes of the northern hemisphere. The southern polar vortex reaches only 0.5 $^{\circ}/\text{yr}$, but it still contains larger angular velocities than elsewhere in the southern hemisphere. We note that equatorially-asymmetric zonal flow outside the tangent cylinder and large symmetric westward polar vortices were found previously by Pais and Hulot (2000) in their time-average zonal core flow.

Zonal azimuthal velocities are correlated/anticorrelated with zonal meridional velocities in the southern/northern hemispheres, respectively, as expected for helical flow. For example, in the northern hemisphere an upwelling is associated with a clockwise vortex in accord with the

helical flow assumption, yielding northward (negative) poloidal flow and eastward (positive) toroidal flow on the northern part of the vortex. Zonal meridional velocities inside the tangent cylinder are equatorward (Fig. 4b), as expected from upwelling (Fig. 4c) below westward polar vortices (Figs. 3b and 4a) in helical flow.

The time-average zonal divergence (Fig. 4c) is anticorrelated with time-average zonal intensity of the non-dipolar normal magnetic flux (Fig. 4d). More specifically, the equatorial intense normal polarity flux patches discussed by Jackson (2003) in Fig. 4d correlate with convergence at the equator (Figs. 3a and 4c), and the Southern Atlantic magnetic field anomaly correlates with mid-latitude divergence in the southern hemisphere. These correlations are consistent with frozen-flux behavior, where magnetic field is concentrated by downwelling and dispersed by upwelling, and suggest that the meridional circulation perturbs the time-average magnetic field from an axisymmetric dipole pattern.

4.1 Thermal wind in the core

Many authors have proposed that lower mantle heterogeneity may control some of the fluid motion in the outer core (Gubbins and Richards, 1986; Bloxham and Jackson, 1990; Zhang and Gubbins, 1992; Glatzmaier et al., 1999; Olson and Christensen, 2002; Christensen and Olson, 2003). One specific proposal is that large-scale core flow, especially the zonal azimuthal part of core flow, is a thermal wind driven by lateral density gradients induced by thermal coupling to the lower mantle (Bloxham and Jackson, 1990; Zhang and Gubbins, 1992; Christensen and Olson, 2003). To test this hypothesis, we analyze the thermal wind equation in spherical coordinates for a thick rotating fluid shell using our core flow and models of mantle- and core-produced density heterogeneity. For simplicity, we ignore the magnetic Lorentz force.

The vorticity equation for an incompressible, steady, inviscid, rotating, non-magnetic fluid is given by Pedlosky (1987),

$$(2\vec{\Omega} \cdot \nabla)\vec{u} = -\frac{\nabla\rho \times \nabla p}{\rho^2} \quad (6)$$

where $\vec{\Omega}$ is the rotation vector, \vec{u} is fluid velocity, ρ is density and p is pressure. Assuming hydrostatic pressure,

$$\nabla p = -\rho g \hat{r} \quad (7)$$

where g is the gravitational acceleration, (6) becomes

$$(2\vec{\Omega} \cdot \nabla)\vec{u} = \frac{g}{\rho}(\nabla\rho \times \hat{r}) \quad (8)$$

The azimuthal component of (8) just below the core-mantle boundary ($r = R$) is

$$\frac{\partial u_\phi}{\partial \theta} - R \cot \theta \frac{\partial u_\phi}{\partial r} = \frac{g_0}{2\Omega\rho_0} \frac{1}{\sin \theta} \frac{\partial \rho}{\partial \theta} \quad (9)$$

where ρ_0 and g_0 are the density and gravitational acceleration at the core-mantle boundary, respectively.

In a thin spherical shell the first term on the left hand side of (9) is negligible with respect to the second term, yielding the form of the thermal wind equation commonly used for the atmosphere and the ocean (e.g. Holton, 1992; Andrews, 2000). In this approximation the meridional density gradient balances radial velocity shear. In the outer core, however, we expect that tangential and radial length-scales are comparable, and both terms on the left hand side of (9) should be considered. The meridional shear $\partial u_\phi / \partial \theta$ can be calculated from our inverted core flow, but we need an independent way to estimate the radial shear $\partial u_\phi / \partial r$ in the core.

Inversions of the horizontal component of the magnetic induction equation using measurements of changes in the horizontal component of the magnetic field on the core-mantle boundary suggest that the vertical shear in the tangential velocity at the top of the core is proportional to the tangential velocity there (Lloyd and Gubbins, 1990; Jackson and Bloxham, 1991). This argument is equivalent to assuming that the surface core flow correlates with deep core flow. Jackson and Bloxham (1991) have proposed that the length-scale of the vertical shear is one half the radius of the core, i.e.

$$\frac{\partial \vec{u}_h}{\partial r} \simeq 2 \frac{\vec{u}_h}{R} \quad (10)$$

Adopting this assumption, (9) becomes

$$\frac{\partial}{\partial \theta} \left(\frac{u_\phi}{\sin^2 \theta} \right) \simeq \frac{g_0}{2\Omega\rho_0} \frac{1}{\sin^3 \theta} \frac{\partial \rho}{\partial \theta} \quad (11)$$

4.2 Thermal coupling with the mantle

Possible mechanisms for core-mantle coupling include thermal, compositional and topographic (Hide, 1967; Gubbins and Richards, 1986; Bloxham and Gubbins, 1987; Loper and Lay, 1995; Schubert et al., 2001). Simple thermal core-mantle coupling assumes that the temperature anomalies at the lower mantle are anticorrelated with the density anomalies at the top of the core (Bloxham and Gubbins, 1987; Bloxham and Jackson, 1990). A second assumption that is often made is that temperature anomalies are anti-correlated to seismic shear velocity anomalies in the lower mantle (Forte and Mitrovica, 2001).

To model thermal coupling with the mantle, we assume density anomalies at the top of the core are proportional to seismic shear velocity anomalies in the lower mantle as follows:

$$\frac{1}{\rho} \frac{\partial \rho}{\partial \theta} \Big|_{core} = \frac{C}{v_s} \frac{\partial v_s}{\partial \theta} \Big|_{mantle} \quad (12)$$

Equation (12) involves several assumptions. First, the sign of C depends on the type of core-mantle coupling (Olson and Christensen, 2002). If thermal core-mantle coupling prevails, we expect $C > 0$, i.e., a positive mantle seismic velocity anomaly produces a positive core density anomaly. If compositional coupling is dominant, we expect $C < 0$, i.e., a positive velocity anomaly produces a negative density anomaly. Second, the relationship between seismic shear velocity to temperature in the lower mantle is currently under debate. For example, a recent study which separated mantle seismic velocity heterogeneity into thermal and chemical contributions argues that most of the buoyancy in the lower mantle is dominated by chemical variations, and the temperature heterogeneity is very different from the seismic velocity heterogeneity there (Trampert et al., 2004).

Figs. 5a and 5b show maps of the lower mantle seismic tomography of Li and Romanowicz (1996) and Masters et al. (1996), hereafter referred to as LR and MJLB, respectively. Both Figs. 5a and 5b were obtained by depth-averaging seismic shear velocity anomalies in the lower mantle from a depth of 2500 km to the core-mantle boundary. The large-scale features common to both models include (1) mid-latitudes of the northern hemisphere are dominated by positive anomalies, whereas low and mid-latitudes of the southern hemisphere are dominated by negative anomalies; (2) large negative anomalies below Africa and the Pacific; and (3) large

positive anomalies below north America, central Asia and Antarctica. The two tomography models differ in some smaller-scale features, which are not important here. Fig. 5c shows the zonal profiles of the seismic shear velocity anomalies. Note that the typical wavelength is larger in the MJLB model, and the magnitude is larger at the LR model. We use these models to calculate $\partial v_s / \partial \theta$ and its zonal average. Equation (12) is then used to connect $\partial \rho / \partial \theta$ at the top of the core with $\partial v_s / \partial \theta$ at the bottom of the mantle. Using $\partial \rho / \partial \theta$ at the top of the core derived this way, we then solve (11) for the core azimuthal flow u_ϕ driven by the mantle.

4.3 Time-average core flow from numerical dynamos

In addition to a mantle origin, the time-average flow shown in Fig. 3 may also have an origin in the core's own dynamics. Convection in the core results in large-scale lateral density gradients, a consequence of the spherical shell geometry and the constraints of Earth's rotation (Olson et al., 1999). A recent study of numerical dynamos with homogeneous core-mantle boundary conditions shows that thermal convection results in a large-scale thermal wind flow, with a predictable pattern and an amplitude that depends only on the buoyancy flux and the rotation rate (Aubert, 2005). Aubert (2005) verified that a scaling law for the amplitude of this zonal flow previously proposed by Aurnou et al. (2003) remains valid in the presence of a magnetic field.

We use a 3D, self-consistent numerical dynamo which solves simultaneously the full magnetohydrodynamics equations in a rotating, convecting sphere (Olson et al., 1999). We used the following parameter values: $Ra = 4E5$, $Ek = 7E - 4$, $Pr = 1$ and $Pm = 5$, where Ra is the Rayleigh number, Ek is the Ekman number, Pr is the Prandtl number and Pm is the magnetic Prandtl number. We assume rigid boundaries with fixed temperatures. To obtain the zonal angular velocity profile, we averaged the solution over 3 magnetic diffusion times. Fig. 6 shows the zonal core flow obtained from the numerical dynamo (depth averaged over 150 km below the outer boundary). Numerical dynamos over a wide range of parameters produce similar time-average zonal flow pattern, although there are significant variations in the zonal flow pattern in individual snapshots.

Fig. 6 shows a snapshot and the time-average zonal temperature and azimuthal velocity

profiles from the numerical dynamo. The basic convection structure consists of two polar plumes and several equatorial plumes. The equatorial plumes wobble around the equator with time, and at any instant the temperature profile deviates from equatorial symmetry (Fig. 6a). However, the time-average positions of equatorial plumes are very close to the equator, and therefore the time-average temperature profile is nearly symmetric with respect to the equator (Fig. 6c). The time-average azimuthal velocity field is mostly a thermal wind flow driven by lateral gradients in the time-average temperature field. The most intense zonal flow is within the inner core tangent cylinder, particularly the westward polar vortex (Figs. 6b and 6d).

4.4 Interpretation of time-average core flow: mantle versus core origins

Fig. 7 compares the zonal parts of core, tomographic, and dynamo flows, respectively. The tomographic flows were scaled and shifted to best fit the core flow. The amplitude of the numerical dynamo zonal flow U_ϕ is related to the buoyancy flux using the following scaling law:

$$U_\phi = Ra_q^{*0.5} = \left[\left(\frac{R_i}{R} \right) \frac{B}{\Omega^3 D^2} \right]^{0.5} \quad (13)$$

where Ra_q^* is the heat flux based Rayleigh number, R_i is the inner core radius, $D = R - R_i$ is the shell thickness and B is the buoyancy flux (Aubert, 2005). Our scaling of U_ϕ corresponds to a buoyancy flux of $\sim 3 \cdot 10^{-12} \text{ m}^2/\text{s}^3$ which is within the range of estimated values for this parameter at the outer core (Aurnou et al., 2003). The error bars in the dynamo flow represent variation in time.

Fig. 7 shows that the dynamo flow can account for most of the zonal core flow at high latitudes. Specifically, the westward polar vortices seen in the core flow are present in the dynamo flow. In addition, the eastward flow at high latitudes outside the tangent cylinder in the dynamo flow is in agreement with eastward motion at similar latitudes in the core flow. However, core dynamics does not readily explain the asymmetry in the westward drift in the core flow. The dynamo flow is practically zero within 50° of the equator, whereas the core flow has substantial westward amplitude, particularly at mid-latitudes in the southern hemisphere. Mantle-driven flow offers an explanation for this asymmetry. The southern hemisphere has a larger westward drift than the northern hemisphere in both tomographic flows. The LR tomographic flow has

the same wavelength and phase as the core flow, and in particular, reproduces the westward jet at $40S$ and the eastward flow at $70N$. Discrepancies between the tomographic and core flows appear mostly in the equatorial region and in mid-latitudes of the northern hemisphere.

Fig. 8 shows results of a test of the mantle-driven thermal wind over the entire core-mantle boundary. Fig. 8a shows the meridional derivative of the seismic velocities from the LR tomography model, and Fig. 8b shows the same quantity based on the thermal wind balance (11) and the azimuthal core flow. The tomographic model has a significant thermal wind in the Pacific hemisphere (Fig. 8a) where the historical secular variation and the core flow are generally quiet (see Figs. 1, 2 and 3a). The opposite relation is found in the Atlantic hemisphere. As a result, the global correlation is poor (Fig. 8c). Possible explanations for the poor global correlation include non-zonal core flow is transient, i.e. the 100 years interval used in this study is marginally inadequate; core-mantle coupling is not just thermal, as we assumed (see Trampert et al., 2004); or thermal wind is an over-simplified model for core flow. It is also possible that over this time interval the global core flow contains transients, but its zonal flow is essentially steady. For example, several studies assumed steady core flow in an azimuthally drifting reference frame (Voorhies and Backus, 1985; Davis and Whaler, 1996; Holme and Whaler, 2001). In the mantle reference frame, the azimuthal component of such a flow is transient, but its zonal component is steady.

Our results have some similarities as well as some differences with other thermal wind interpretations of mantle-driven core flow. Bloxham and Jackson (1990) used the thermal wind equation to diagnose mantle density anomalies consistent with a model of core flow. Their results reproduce the thermal anomaly in the mantle below the Southern Indian Ocean associated with the circulatory core flow there. At that region, our time-average core flow contains the same feature (Fig. 3a), and our mantle-driven thermal wind correlation is good (Figs. 8a and 8b). However, globally our core flow and the core flow of Bloxham and Jackson (1990) do not explain well the seismic data by thermal wind. Comparisons can also be made between our results and thermal wind models from numerical dynamos with heterogeneous boundary conditions. Zhang and Gubbins (1992) investigated the effect of thermal wind driven by mantle heterogeneity in a kinematic dynamo model. They found that core flow structure is shifted in longitude with respect to mantle density anomalies, so that core upwellings occur where the

mantle density anomalies change sign. We find this type of correlation in a few places, for example below the Southern Indian Ocean and below the Northern Atlantic Ocean (Figs. 3a and 5a). Olson and Christensen (2002) applied the MJLB lower mantle tomography model as a boundary condition in numerical dynamos with thermal core-mantle coupling. Their time-average flow contains a southern hemisphere vortex similar to ours, but the circulation in their dynamo model below North America is the reverse of ours. The discrepancy below North America could be because our core flow is transient there, or the tomographic dynamo of Olson and Christensen (2002) has the wrong core-mantle coupling in that location.

In summary, several important features of our time-average zonal core flow are in agreement with thermal wind driven by lower mantle lateral heterogeneities, while other structures appear to have their origin in the core's own dynamics. Likely mantle-driven features include hemispherical asymmetry in the westward drift, westward polar vortices, and a westward jet in the southern hemisphere at the latitude predicted by thermal coupling with the mantle. The equatorial asymmetry of the core flow at mid-latitudes appears to have a mantle origin, because the expected core-driven zonal flow is both very weak and highly symmetric there. The westward polar vortices and eastward flow near latitudes $50N$ and $50S$ may have a core origin. Globally, the azimuthal core flow is not well-correlated with mantle tomographic thermal wind. Possible explanations of this poor correlation include the short record used for averaging the core flow, non-thermal wind core flow components, and our over-simplified core-mantle coupling model. However, our results are consistent with the interpretation that the zonal part of the 100 year average core flow approximates steady-state flow at the top of the core.

5 Time-dependent core flow

Time-dependent core flow implies changes in the angular momentum of the core, which can be compared with observations of length-of-day variations. Fig. 9 shows the zonal angular velocity profiles from our core flow snapshots at 5 year intervals between 1895-1985. The center of the envelope of curves represents the time-average zonal flow, and the width of the envelope is a measure of its time-dependence. Statistics of the time-dependent flow are given in Table 1. Several points are worth emphasizing here. First, the ratio of standard deviation

to mean of the rms velocities of snapshots, which represents the ratio of time-dependent to time-average parts of our core flow, is 8.6%. Second, time-dependence is generally larger in the northern hemisphere; indeed the drift reverses its direction in some years. The westward drift at mid-latitudes of the southern hemisphere is more persistent in time and its peak angular velocity varies between $0.19 - 0.33 \text{ }^\circ/\text{yr}$. Third, the polar vortices are evident in all profiles, despite the resolution problems in the relatively small polar cap area. A strong westward polar vortex ($0.95 - 1.80 \text{ }^\circ/\text{yr}$) is evident in the northern polar cap, and a less intense polar vortex ($0.22 - 0.83 \text{ }^\circ/\text{yr}$) is evident in the south.

Residual zonal flows were obtained by subtracting the time-average flow (Fig. 3b) from the zonal flow snapshots (Fig. 9). The parts of the residual flow symmetric with respect to the equator were then calculated. These equatorially-symmetric residual zonal flows represent the part of the core flow contributing to changes in the core's angular momentum. The ratio of symmetric to anti-symmetric parts of the residual zonal flows is shown in Fig. 10. The most symmetric zonal flow occurred at 1970, and the least symmetric zonal flow occurred at 1910. This is in agreement with previous studies, which found that core flows are more symmetric after 1970 than before (Jault et al., 1988; Jackson et al., 1993).

5.1 Length-of-day variations theory

Observations of length-of-day variations can be related to changes in the core's angular momentum, assuming conservation of angular momentum in the core-mantle system. The Earth changes its rotation rate on several time-scales, from seasonal fluctuations originating in the atmosphere (Eubanks et al., 1985) to geological time-scale fluctuations originating in the mantle (Munk and McDonald, 1960). Well-known contributions to length-of-day variations include lunar tidal dissipation ($+2.3 \pm 0.05 \text{ ms} \cdot \text{cy}^{-1}$) and postglacial rebound in polar regions ($-0.6 \pm 0.1 \text{ ms} \cdot \text{cy}^{-1}$) which combine to a $1.7 \pm 0.15 \text{ ms} \cdot \text{cy}^{-1}$ secular increase in the length-of-day over the last 2700 years (Stephenson and Morrison, 1995). Only the decadal variations are usually attributed to time-dependent differential rotation in Earth's liquid outer core (Jault et al., 1988; Jackson et al., 1993; Jackson, 1997; Pais and Hultot, 2000; Hide et al., 2000; Holme and Whaler, 2001).

Calculation of changes in the core's angular momentum from knowledge of core flow just below the core-mantle boundary requires projection of that flow into the volume of the outer core. Bullard and Gellman (1954) suggested that zonal core flow is geostrophic and consists of cylinders in solid body rotation about the Earth's axis of rotation. Taylor (1963) showed that for an inviscid fluid, steady motions of this type are possible when the couple exerted by Lorentz forces on those concentric cylinders vanishes (a condition known as Taylor's constraint). This cylindrical projection was used by Jault et al. (1988) to compare observed versus calculated length-of-day variations. The exact coupling mechanism between the core and the mantle is disputed. Jault and LeMouél (1989) calculated angular momentum transfer between the core and the mantle assuming topographic torques linked with rigid body flow along such cylinders. Later, Jault and LeMouél (1991) argued that, if the amplitude of core-mantle boundary topography is as large as suggested by seismologists, then topographic torque is too large to account for length-of-day variations. They proposed an electromagnetic torque as a coupling mechanism. Regardless of the coupling mechanism to the mantle, most studies agree that the angular momentum-containing slow motion within the core is along concentric cylinders about the Earth's axis of rotation (Jault et al., 1988; Jackson et al., 1993; Jackson, 1997; Pais and Hulot, 2000).

Changes in length-of-day δT caused by core motions can be expressed as

$$\delta T(t) = \frac{T_0^2(I_c + I_m)}{2\pi} \delta J_z(t) \quad (14)$$

where $I_c = 0.85 \cdot 10^{37} \text{ kg} \cdot \text{m}^2$ and $I_m = 7.2 \cdot 10^{37} \text{ kg} \cdot \text{m}^2$ are the moments of inertia of the core and the mantle respectively, $T_0 = 24$ hours, and

$$\delta J_z(t) = 2\pi \int_{R_i}^R \int_0^\pi \rho(r) \delta \omega_\phi(r, \theta, t) r^4 \sin^3 \theta d\theta dr \quad (15)$$

is the time-residual angular momentum component in the direction of the rotation axis associated with the core motions relative to the mantle (Jackson et al., 1993). In (15) R_i is the radius of the inner core boundary, R is the radius of the core-mantle boundary, ρ is core density, and $\delta \omega_\phi$ is the zonal angular velocity residual, the deviation of the profiles $\omega_\phi(R, \theta, t)$ shown in Fig. 9 from the time-average profile shown in Fig. 3b.

To compute $\delta J_z(t)$, the time-average zonal core flow is subtracted from $\omega_\phi(R, \theta, t)$, and the even (symmetric with respect to the equator) angular velocity time residual $\delta \omega_\phi(R, \theta, t)$ is

found. To project along concentric cylinders in a spherical coordinate system, the following expression is used:

$$\delta\omega_\phi(r, \theta, t) = \delta\omega_\phi(R, \theta^*, t) \quad (16)$$

where $\theta^* = \sin^{-1}(\frac{r}{R} \sin \theta)$ is the co-latitude where an axial cylinder passing through the point (r, θ) intersects the core-mantle boundary.

Although previous studies have ignored the depth-dependent density in the outer core (e.g. Jault et al., 1988; Jackson et al., 1993; Jackson, 1997; Pais and Hulot, 2000), we use the radial density profile model of Dziewonski and Anderson (1981) to evaluate the radial density profile in (15). Note that the inner core is not included in (15). The inner core has a small volume fraction and even smaller moment of inertia with respect to the whole core (Stacey, 1992), and therefore its contribution to the angular momentum of the entire core is negligible.

5.2 Comparison with observed length-of-day variations

Fig. 11 shows the δT calculated from our surface core flow and (14) - (16) versus the observed length-of-day variations since 1895. A linear trend of $1.7 \text{ ms} \cdot \text{cy}^{-1}$ has been subtracted from the observations to remove the secular increase in Earth's rotation rate due to the long-term causes listed above. Although our calculated length-of-day variations have a larger amplitude than observed, there is a reasonable agreement in terms of general trend and peak-to-peak-correlation.

Some previous studies have obtained better fits between calculated and observed length-of-day variations than ours, especially the amplitude of the variation (Jackson et al., 1993; Jackson, 1997). However, those fits were obtained by linking the core flow at different epochs. Jackson (1997) linked different epochs by minimizing the temporal variations of the flow, and Holme (1998) linked different epochs by minimizing the length-of-day variations misfit. In addition, some previous studies improved their fit by using time-dependent spectral tapering to account for the increasing uncertainty in older data (Jackson, 1997; Pais and Hulot, 2000). We do not constrain our snapshot flows these ways. Instead we invert for the core flow at each epoch independently, so our snapshot flows are uncoupled. In addition, we keep our model parameters fixed over time. Because our snapshot flows are not linked and our model

parameters are time-independent, we view the length-of-day comparison as an independent test of our core flow solution.

5.3 Torsional oscillations model for time-dependent core flow

The correlation between the observed and calculated length-of-day variations does not answer the question of what mechanism is responsible for the time-dependent motions in the core, but many authors have argued that the mechanism is torsional oscillations. Braginsky (1970) provided a theoretical basis for torsional oscillations within the outer core, and estimated that these oscillations have a period of about 60 years. Jault et al. (1996) argued that core-mantle angular momentum exchange is a by-product of angular momentum exchange among different cylinders inside the outer core, through torsional oscillations. Zatman and Bloxham (1997) fitted the even residual zonal surface flow for the time interval 1900-1990 to a torsional oscillations model and found two damped waves with periods of 76.2 and 52.7 years. Bloxham et al. (2002) assumed steady acceleration to fit the time interval 1957-2001 and found three damped waves with periods of 45, 20 and 13 years. They also argued that torsional oscillations are the mechanism responsible for the observed geomagnetic jerks, which are abrupt changes in the secular acceleration of the geomagnetic field.

Following Zatman and Bloxham (1997) and Bloxham et al. (2002), we fit a torsional oscillations model to the time-dependent part of our zonal core flow. We use a two-wave model for the equatorially-symmetric time-dependent zonal velocity

$$\delta u_\phi(\theta, t) = A_1(\theta) \cos\left(\frac{2\pi}{T_1}t + \gamma_1(\theta)\right) + A_2(\theta) \cos\left(\frac{2\pi}{T_2}t + \gamma_2(\theta)\right) \quad (17)$$

where A , T and γ are the amplitudes, periods and phases of the two waves. Figs. 12a and 12b show δu_ϕ from our core flow model and from the least-squares fit to (17), respectively. The best-fit periods are $T_1 = 88.3$ years and $T_2 = 48.3$ years. Note that the largest amplitudes occur at high latitudes and in the equatorial region. The misfit is shown in Fig. 12c. The ratio of the misfit (Fig. 12c) rms to the core flow (Fig. 12a) rms is 0.22.

The average of our periods, 68.3 years, as well as the average of the two periods found by Zatman and Bloxham (1997), 64.5 years, are very close to the 60 years period estimated by

Braginsky (1970). Our high frequency wave has a period close to the one found by Zatman and Bloxham (1997), but our low frequency wave has a larger period than theirs. In contrast, the periods found by Bloxham et al. (2002) are substantially smaller than ours.

Fig. 13 shows the latitude-dependent wave amplitudes and phases. Both waves have local amplitude maxima at the equator, but wave 1 also has a significant local maximum near latitude 62. These are not simple standing or propagating waves, since their phases are latitude-dependent. We searched for models with simpler phase relationships, unsuccessfully. For a model with the same periods $T_1 = 88.3$ years and $T_2 = 48.3$ years and $\gamma_1 = 0$, the quality of fit decreases only by 2%, but γ_2 still depends strongly on latitude. We then set both phases constant for the period of time 1940-1985 and found best-fit in periods of $T_1 = 88.4$ years and $T_2 = 59.8$ years, and the quality of fit decreases by 16%. The similarity of the periods (especially T_1) obtained this way to those obtained for the whole 1895-1985 time interval demonstrates they are not a consequence of the sampling interval, but are robust features of the symmetric residual zonal velocities. In summary, we find that the symmetric zonal part of the time-dependent core flow can be successfully fitted using a sum of two harmonic functions with constant periods, and this may be evidence to torsional oscillations at the Earth's core on decadal time-scales. We found that the periods are robust, but the complex phase relationships indicate that these torsional oscillations are not simple standing or propagating waves.

6 Summary

We have inverted geomagnetic secular variation data for the fluid flow below the core-mantle boundary at 5 year intervals between 1895-1985. We decompose the core flow into time-average and time-dependent parts. The time-average zonal core flow, which may represent a long-term steady flow at the top of the core, is compared with models of thermal wind at the top of the core driven by density anomalies originating in the core and the mantle. Core-origin flow can account for large westward polar vortices and eastward flow at high latitudes outside the tangent cylinder. Mantle-driven thermal wind seems to account for the hemispherical asymmetry at low and mid-latitudes. The time-dependent part of our core flow is in overall agreement with decade-scale length-of-day variations, and a torsional oscillations

model with periods near 88 and 48 years but complex phase relationships provides an adequate fit to this part of our core flow.

Acknowledgments

This research was supported by a grant from the Geophysics Program of the National Science Foundation.

References

- Amit, H., Olson, P., 2004. Helical core flow from geomagnetic secular variation. *Phys. Earth Planet. Inter.*, 147, 1-25, doi:10.1016/j.pepi.2004.02.006.
- Andrews, D.G., 2000. *Atmospheric physics*. Cambridge University Press, Cambridge, UK, 229 pp.
- Aubert, J., 2005. Steady zonal flows in spherical shell fluid dynamos. *J. Fluid Mech.*, submitted.
- Aurnou, J., Andreadis, S., Zhu, L., Olson, P., 2003. Experiments on convection in Earth's core tangent cylinder. *Earth and Planet. Sci. Lett.*, 212, 119-134.
- Backus, G.E., 1968. Kinematics of geomagnetic secular variation in a perfectly conducting core. *Phil. Trans. R. Soc. Lond.*, A263, 239-266.
- Backus, G.E., LeMouél, J.-L., 1986. The region on the core mantle boundary where a geostrophic velocity field can be determined from frozen flux magnetic data. *Geophys. J. R. Astron. Soc.*, 85, 617-628.
- Bloxham, J., 1989. Simple models of fluid flow at the core surface derived from geomagnetic field models. *Geophys. J. Int.*, 99, 173-182.
- Bloxham, J., 1992. The steady part of the secular variation of the Earth's magnetic field. *J. Geophys. Res.*, 97, 19565-19579.
- Bloxham, J., Gubbins, D., 1987. Thermal core-mantle interactions. *Nature*, 325, 511-513.
- Bloxham, J., Jackson, A., 1990. Lateral temperature variations at the core-mantle boundary deduced from the magnetic field. *Geophys. Res. Lett.*, 17, 1997-2000.
- Bloxham, J., Jackson, A., 1991. Fluid flow near the surface of Earth's outer core. *Rev. Geophys.*, 29, 97-120.
- Bloxham, J., Jackson, A., 1992. Time-dependent mapping of the magnetic field at the core-mantle boundary. *J. Geophys. Res.*, 97, 19565-19579.

- Bloxham, J., Zatman, S., Dumberry, M., 2002. The origin of geomagnetic jerks. *Nature*, 420, 65-68.
- Bullard, E.C., Freedman, C., Gellman, H., Nixon, J., 1950. The westward drift of the Earth's magnetic field. *Phil. Trans. Roy. Soc., London A243*, 67-92.
- Bullard, E.C., Gellman, H., 1954. Homogeneous dynamos and terrestrial magnetism. *Phil. Trans. R. Soc. Lond., A 247*, 213-278.
- Chulliat, A., Hulot, G., 2000. Local computation of the geostrophic pressure at the top of the core. *Phys. Earth Planet. Inter.*, 59, 259-287.
- Christensen, U. R., Olson P., 2003. Secular variation in numerical geodynamo models with lateral variations of boundary heat flow. *Phys. Earth Planet. Inter.*, 138, 39-54.
- Christensen, U. R., Tilgner, A., 2004. Power requirement of the geodynamo from ohmic losses in numerical and laboratory dynamos. *Nature*, 429, 169-171, doi: 10.1038/nature02508.
- Davis, R.G., Whaler, K.A., 1996. Determination of a steady velocity in a rotating frame of reference at the surface of the Earth's core. *Geophys. J. Int.*, 126, 92-100.
- Dziewonski, A.M., Anderson, D.L., 1981. Preliminary reference Earth model. *Phys. Earth Planet. Inter.*, 25, 297-356.
- Eubanks, T.M., Steppe, J.A., Dickey, J.O., Callahan, P.S., 1985. A spectral analysis of the Earth's angular momentum budget. *J. Geophys. Res.*, 90, 5385-5404.
- Forte, A.M., Mitrovica, J. X., 2001. Deep-mantle high-viscosity flow and thermochemical structure inferred from seismic and geodynamic data. *Nature*, 410, 1049-1056.
- Gire, C., LeMouél, J.-L., Madden, T., 1986. Motions of the core surface derived by SV data. *Geophys. J. R. Astron. Soc.*, 84, 1-29.
- Gire, C., LeMouél, J.-L., 1990. Tangentially geostrophic flow at the core-mantle boundary compatible with the observed geomagnetic secular variation: The large-scale component of the flow. *Phys. Earth Planet. Inter.*, 59, 259-287.

- Glatzmaier, G., Coe, R., Hongre, L. and Roberts, P., 1999. The role of the earth's mantle in controlling the frequency of geomagnetic reversals. *Nature*, 401, 885-890.
- Gubbins, D., 1982. Finding core motions from magnetic observations. *Philos. Trans. R. Soc. Lond., Ser., A* 306, 249-256.
- Gubbins, D., Richards, M., 1986. Coupling of the core dynamo and mantle: thermal or topographic? *Geophys. Res. Lett.*, 13, 1521-1524.
- Hide, R., 1967. Motions of the earth's core and mantle and variations of the main geomagnetic field. *Science*, 157, 55-56.
- Hide, R., Boggs, D.H., Dickey, J.O., 2000. Angular momentum fluctuations within the Earth's liquid core and torsional oscillations of the core-mantle system. *Geophys. J. Int.*, 143 777-786.
- Holme, R., 1998. Electromagnetic core-mantle coupling-I. Explaining decadal changes in the length of day. *Geophys. J. Int.*, 132, 167-180.
- Holme, R., Whaler, K.A., 2001. Steady core flow in an azimuthally drifting reference frame. *Geophys. J. Int.*, 145, 560-569.
- Holton, J.R., 1992. An introduction to dynamic meteorology. Academic Press, San Diego, US, 511 pp.
- Hulot, G., Eymin, C., Langlais, B., Manda, M., Olsen, N., 2002. Small-scale structure of the geodynamo inferred from Oersted and Magsat satellite data. *Nature*, 416, 620-623.
- Jackson, A., Bloxham, J., Gubbins, D., 1993. Time-dependent flow at the core surface and conservation of angular momentum in the coupled core-mantle system. In: LeMouél, J.-L., Smylie, D.E., Herring, T. (Eds.), *Dynamics of Earth's deep interior and Earth rotation*, Geophysical Monograph 72 IUGG Vol. 12. pp. 97-107.
- Jackson, A., Bloxham, J., 1991. Mapping the fluid flow and shear near the core surface using the radial and horizontal components of the magnetic field. *Geophys. J. Int.*, 105, 199-212.

- Jackson, A., 1997. Time-dependency of tangentially geostrophic core surface motions. *Phys. Earth Planet. Inter.*, 103, 293-311.
- Jackson, A., 2003. Intense equatorial flux spots on the surface of the Earth's core. *Nature*, 424, 760-763.
- Jault, D., Gire, C., LeMouél, J.-L., 1988. Westward drift, core motions and exchanges of angular momentum between core and mantle. *Nature*, 333, 353-356.
- Jault, D., Hulot, G., LeMouél, J.-L., 1996. Mechanical core-mantle coupling and dynamo modeling. *Phys. Earth Planet. Inter.*, 98, 187-191.
- Jault, D., LeMouél, J.-L., 1989. The topographic torque associated with a tangentially geostrophic motion at the core surface and inferences on the flow inside the core. *Geophys. Astrophys. Fluid Dynam.*, 48, 273-296.
- Jault, D., LeMouél, J.-L., 1991. Exchange of angular momentum between the core and the mantle. *J. Geomag. Geoelectr.*, 43, 111-129.
- LeMouél, J.-L., 1984. Outer core geostrophic flow and secular variation of Earth's magnetic field. *Nature*, 311, 734-735.
- Li, X., Romanowicz, B., 1996. Global Mantle Shear-Velocity Model Developed Using Non-linear Asymptotic Coupling Theory. *J. Geophys. Res.*, 101, B10, 22,245-22,272.
- Lloyd, D., Gubbins, D., 1990. Toroidal fluid motion at the top of Earth's core. *Geophys. J. Int.*, 93, 521-526.
- Loper D.E., Lay, T., 1995. The Core-Mantle Boundary Region. *J. Geophys. Res.*, 100, 6397-6420.
- Masters, G., Johnson, S., Laske, G., Bolton H., 1996. A shear-velocity model of the mantle. *Phil. Trans. R. Soc. Lond.*, A 354, 1385-1411.
- Munk, W.H., Macdonald, G.J.F., 1960. *The rotation of the Earth*. Cambridge University Press, Cambridge, UK, 323 pp.

- Olson, P., Aurnou, J., 1999. A polar vortex in the Earth's core. *Nature*, 402, 170-173.
- Olson, P., Christensen, U.R., 2002. The time averaged magnetic field in numerical dynamos with nonuniform boundary heat flow, *Geophys. J. Int.*, 151, 809-823.
- Olson, P., Christensen, U.R. and Glatzmaier, G.A., 1999. Numerical modeling of the geodynamo: Mechanisms of field generation and equilibration. *J. Geophys. Res.*, 104, 10,383-10,404.
- Pais, A., Hulot, G., 2000. Length of day decade variations, torsional oscillations and inner core superrotation: evidence from recovered core surface zonal flows. *Phys. Earth Planet. Inter.*, 118, 291-316.
- Pais, A., Oliveira, O., Nogueira, F., 2004. Nonuniqueness of inverted CMB flows and deviations from tangential geostrophy. *J. Geophys. Res.*, 109, doi:10.1029/2004JB003012.
- Roberts, P.H., Scott, S., 1965. On analysis of the secular variation. *J. Geomagn. Geoelectr.*, 17, 137-151.
- Schubert, G., Turcotte, D., Olson, P., 2001. *Mantle Convection in the Earth and Planets*. Cambridge University Press, Cambridge, UK, 940 pp.
- Stacey, F., 1992. *Physics of the Earth*. Brookfield Press, Brisbane, Australia.
- Stephenson, F.R., Morrison, L.V., 1995. Long-term fluctuation in the Earth's rotation-700 B.C. to A.D. 1990. *Phil. Trans. R. Soc. Lond., A*, 351, 165-202.
- Taylor, J.B., 1963. The magneto-hydrodynamics of a rotating fluid and the earth's dynamo problem. *Proc. R. Soc., A*, 274, 274-283.
- Trampert, J., Deschamps, F., Resovsky, J., Yuen, D., 2004. Probabilistic Tomography Maps Chemical Heterogeneities Throughout the Lower Mantle. *Science*, 306, 853-856, doi: 10.1126/science.11101996.
- Voorhies, C. V., 1986. Steady flows at the top of Earth's core derived from geomagnetic field models. *J. Geophys. Res.*, 91, 12,444-12,466.

Voorhies, C. V., Backus, G.E., 1985. Steady flows at the top of the core from geomagnetic-filed models - the steady motions theorem. *Geophys. Astrophys. Fluid Dyn.*, 32, 163-173.

Waler, K. A., 1980. Does the whole of Earth's core convect? *Nature*, 287, 528-530.

Zatman, S., Bloxham, J., 1997. Torsional oscillations and the magnetic field within the Earth's core. *Nature*, 388, 760-763.

Zhang, K., Gubbins, D., 1992. On convection in the earth's core driven by lateral temperature variations in the lower mantle. *Geophys. J. Int.*, 108, 247-255.

Figure captions

Figure 1 Radial magnetic field and secular variation on the core-mantle boundary at 1900, 1925, 1950 and 1975 from core field model of Bloxham and Jackson (1992). Grey scale represents absolute values, solid lines are positive, dotted lines are negative. The secular variation is the central difference between magnetic field snapshots 10 years apart.

Figure 2 Core flow below the core-mantle boundary for the years 1900 (a), 1925 (b), 1950 (c) and 1975 (d). Contours are streamlines of the toroidal flow; grey scale represents absolute upwelling value with + and - signs indicating upwelling and downwelling, respectively.

Figure 3 Time-average core flow for 1895-1985, and time-average zonal angular velocity for the same time period. Contours in (a) are streamlines of the toroidal flow; grey scale represents absolute upwelling value with + and - signs indicating upwelling and downwelling, respectively.

Figure 4 Time-average zonal azimuthal velocity (a), meridional velocity (b), and divergence (c) of the core flow and non-dipolar magnetic flux intensity (d), all for 1895-1985.

Figure 5 Lower mantle tomography models of LR (a) and MJLB (b), averaged from 2500 km depth to the core-mantle boundary. Grey scale represents absolute values, solid lines are positive seismic shear velocity anomalies, dotted lines are negative anomalies. Corresponding zonal averages are shown in (c).

Figure 6 Zonal temperature (a) and azimuthal velocity (b) from a snapshot, and time-average zonal temperature (c) and azimuthal velocity (d), from a numerical dynamo with $Ra = 4E5$, $Ek = 7E - 4$, $Pr = 1$ and $Pm = 5$. In (b) and (d) solid lines are positive zonal azimuthal velocities (eastward) and dotted lines are negative velocities (westward). Maximum non-dimensional velocities are $2.84Re$ in (b) and $2.43Re$ in (d), where Re is the Reynolds number.

Figure 7 Zonal angular velocities from time-average core flow (solid + x), dynamo flow (solid + error bars), LR tomographic flow (dotted), and MJLB tomographic flow (dashed).

Error bars in dynamo flow represent variation in time.

Figure 8 Meridional derivatives of seismic shear velocities derived from lower mantle tomography model of LR (a), time-average azimuthal core velocities and thermal wind (b), and their correlation (c). Grey scale in (a) and (b) represents absolute values, solid lines are positive seismic shear velocity gradients, dotted lines are negative velocity gradients.

Figure 9 Core flow angular velocity profiles for 1895-1985 in 5 years intervals.

Figure 10 Ratio of symmetric to anti-symmetric zonal residual angular velocities for 1895-1985 in 5 years intervals.

Figure 11 Observed versus calculated length-of-day variations. A linear trend of $1.7 \text{ m.s} \cdot \text{cy}^{-1}$ has been removed from the observations.

Figure 12 Core flow (a), two-wave model (b); and misfit between core flow and two-wave model (c).

Figure 13 Torsional oscillations model wave parameters.

Table 1

Epoch	\vec{u}_h		$\langle u_\phi \rangle$		$\langle u_\theta \rangle$		$\nabla_h \cdot \vec{u}_h$	
	max	rms	max	rms	max	rms	range	rms
1895	105.59	11.94	9.54	2.94	1.46	0.53	-0.16,0.14	0.056
1900	110.40	12.45	10.13	3.08	1.63	0.54	-0.15,0.16	0.062
1905	125.98	13.18	10.73	3.40	1.79	0.56	-0.13,0.17	0.068
1910	132.01	14.18	11.88	3.92	1.93	0.66	-0.17,0.19	0.073
1915	128.66	14.77	13.61	4.53	2.11	0.77	-0.19,0.21	0.077
1920	123.62	14.74	15.09	4.96	2.36	0.90	-0.23,0.23	0.083
1925	120.96	14.71	15.95	5.42	2.55	1.00	-0.27,0.24	0.091
1930	153.94	14.60	16.22	6.12	2.70	1.07	-0.31,0.25	0.100
1935	146.95	13.05	14.31	6.16	2.49	1.01	-0.30,0.21	0.094
1940	145.09	13.74	14.79	7.05	2.50	1.04	-0.30,0.21	0.098
1945	149.57	14.44	15.13	7.40	2.51	1.06	-0.30,0.21	0.099
1950	118.34	12.50	12.95	5.67	1.81	0.78	-0.21,0.17	0.074
1955	100.02	11.88	12.60	5.03	1.40	0.59	-0.13,0.17	0.058
1960	114.63	11.78	12.50	5.31	1.14	0.45	-0.08,0.19	0.053
1965	125.98	11.61	12.08	5.77	1.03	0.41	-0.07,0.22	0.054
1970	120.47	11.44	11.60	5.57	1.07	0.43	-0.08,0.25	0.057
1975	101.65	11.72	11.79	4.96	1.22	0.51	-0.13,0.28	0.062
1980	82.58	11.94	12.31	4.27	1.35	0.58	-0.19,0.30	0.066
1985	92.77	11.99	12.52	3.69	1.43	0.64	-0.24,0.31	0.072
Standard deviation	15.02	1.11	1.54	0.99	0.49	0.20	0.07,0.04	0.013
Time-average	78.69	11.27	12.09	3.60	1.74	0.63	-0.18,0.17	0.063

Table 1: Core flow statistics. $\langle \rangle$ denotes zonal average, rms is areal-average of absolute velocities; standard deviation is with respect to the mean of the epoch values; time-average velocities are from the average of the potentials Ψ and Φ at all epochs. Maximum zonal values are outside the tangent cylinder; maximum zonal azimuthal velocity is westward, maximum zonal meridional velocity is northward; positive divergence is upwelling and negative divergence is downwelling. All velocities are km/yr; divergence is 1/century.

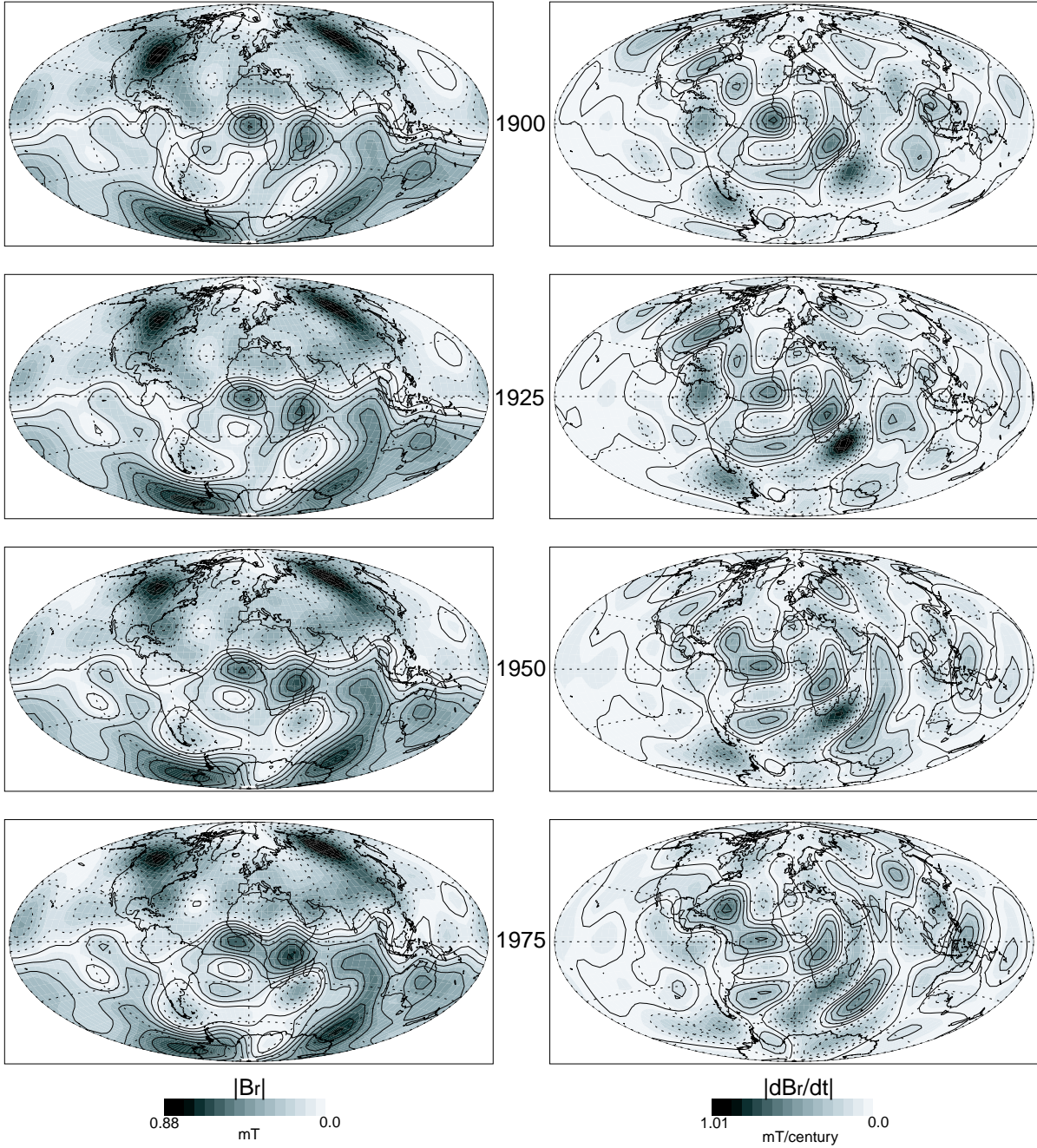


Fig. 1

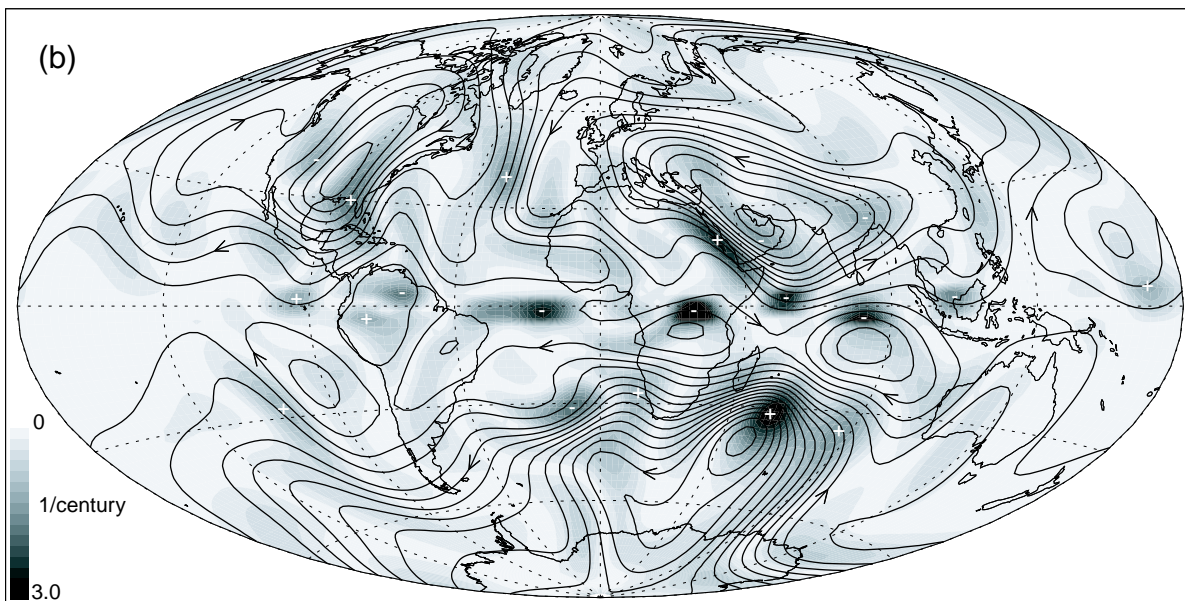
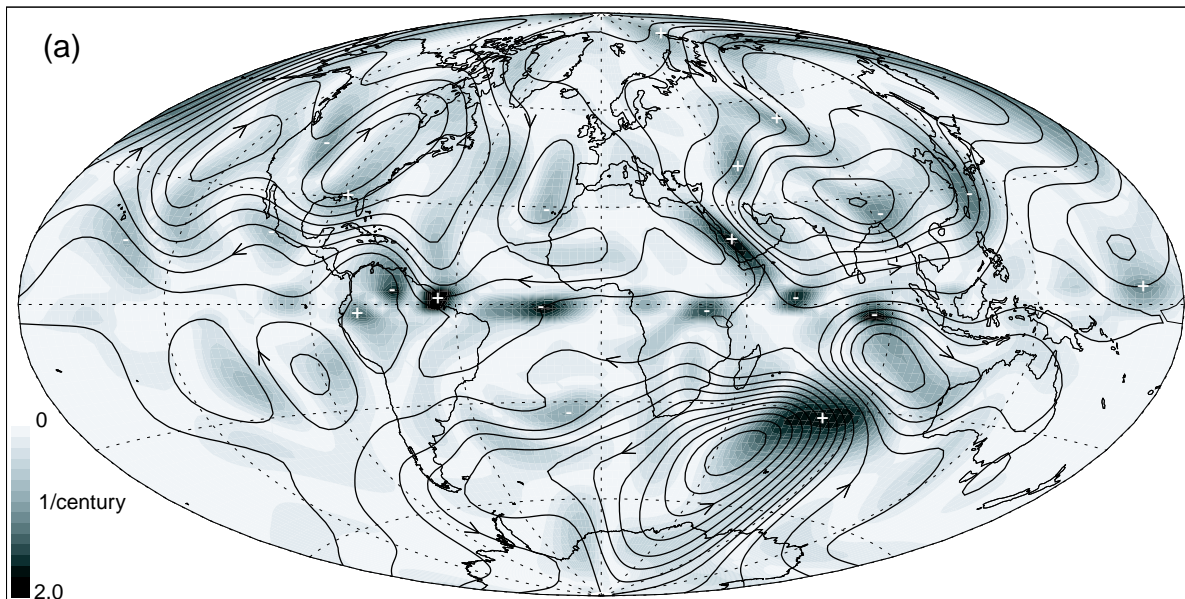


Fig. 2

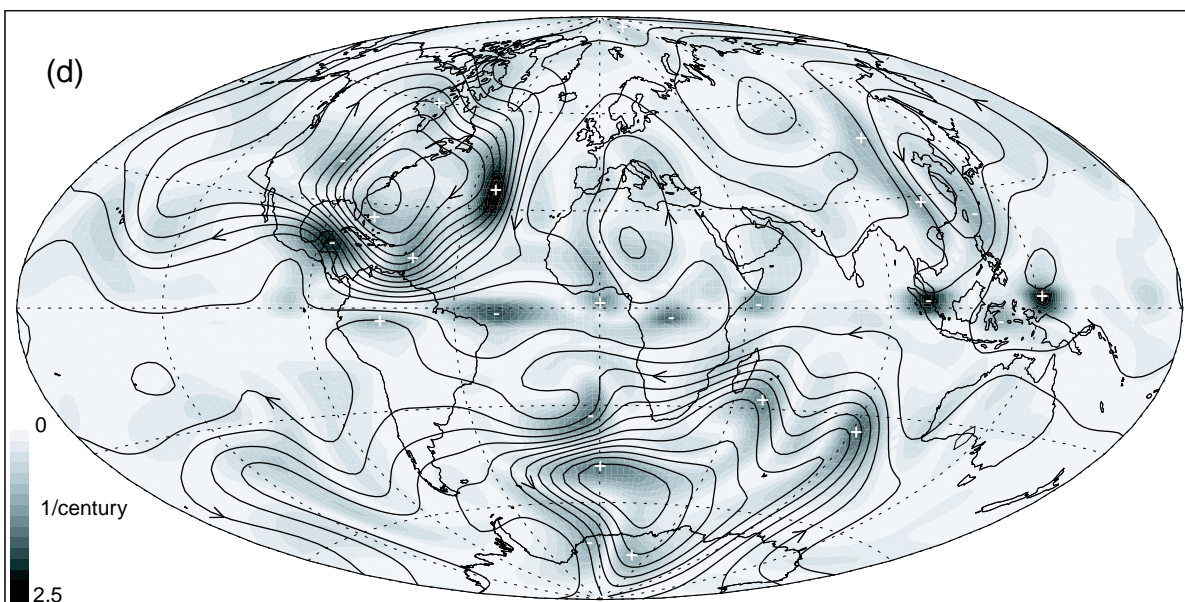
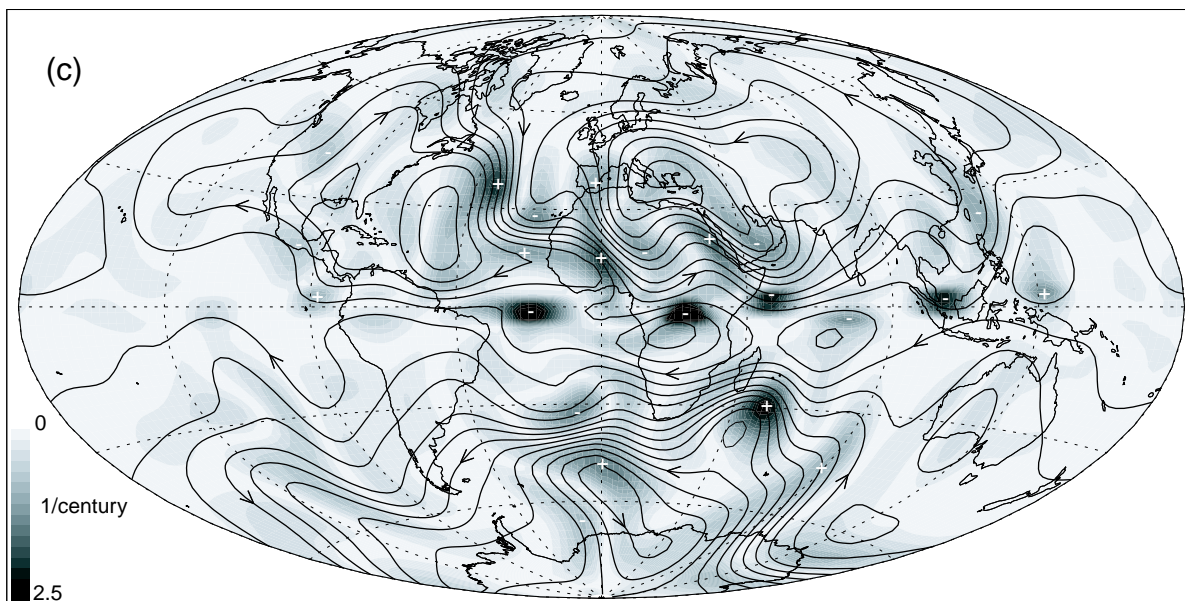


Fig. 2 cont'

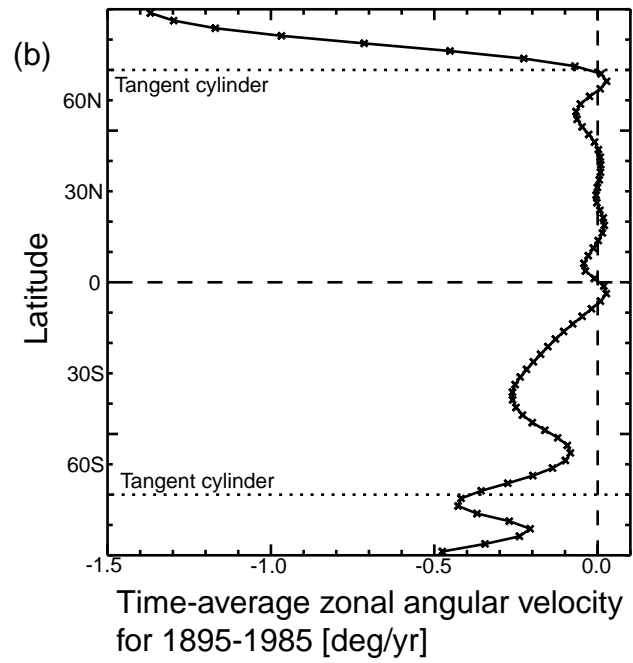
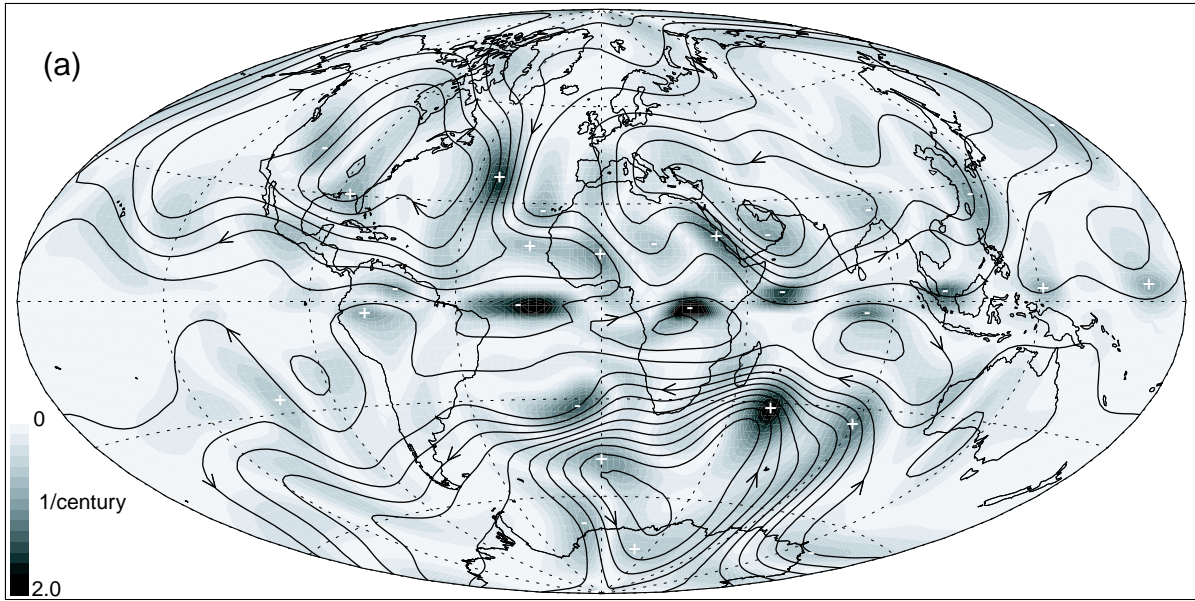


Fig. 3

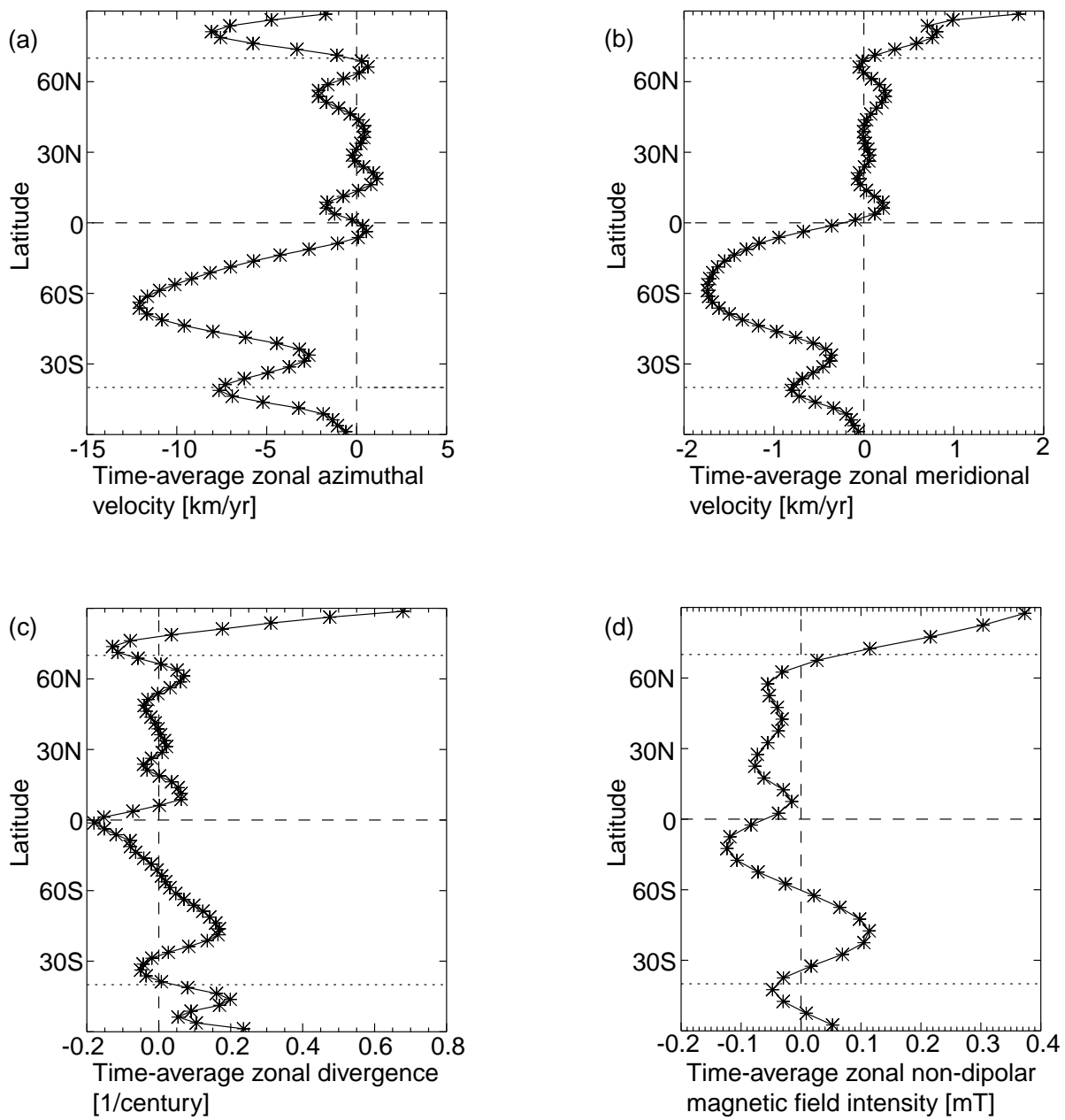


Fig. 4

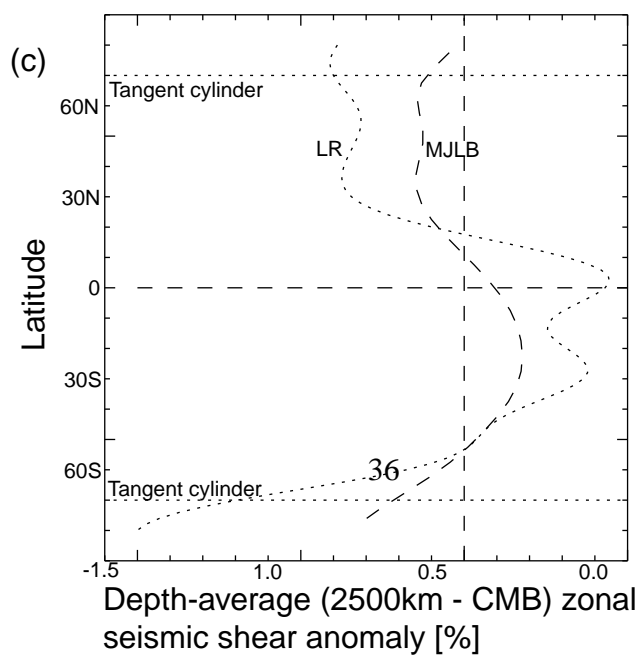
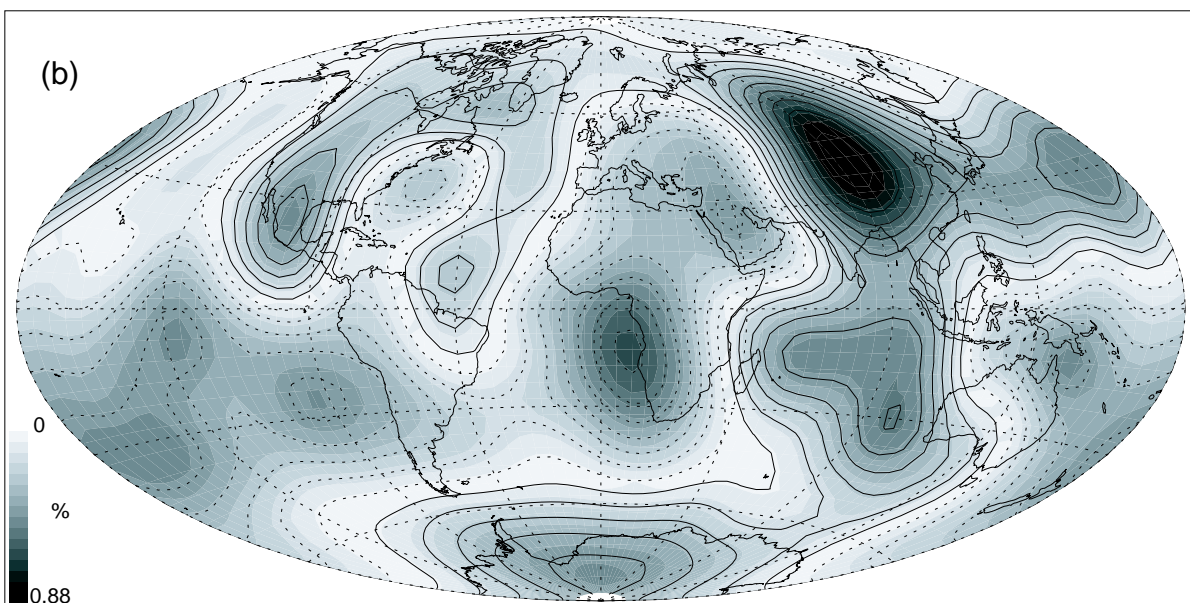
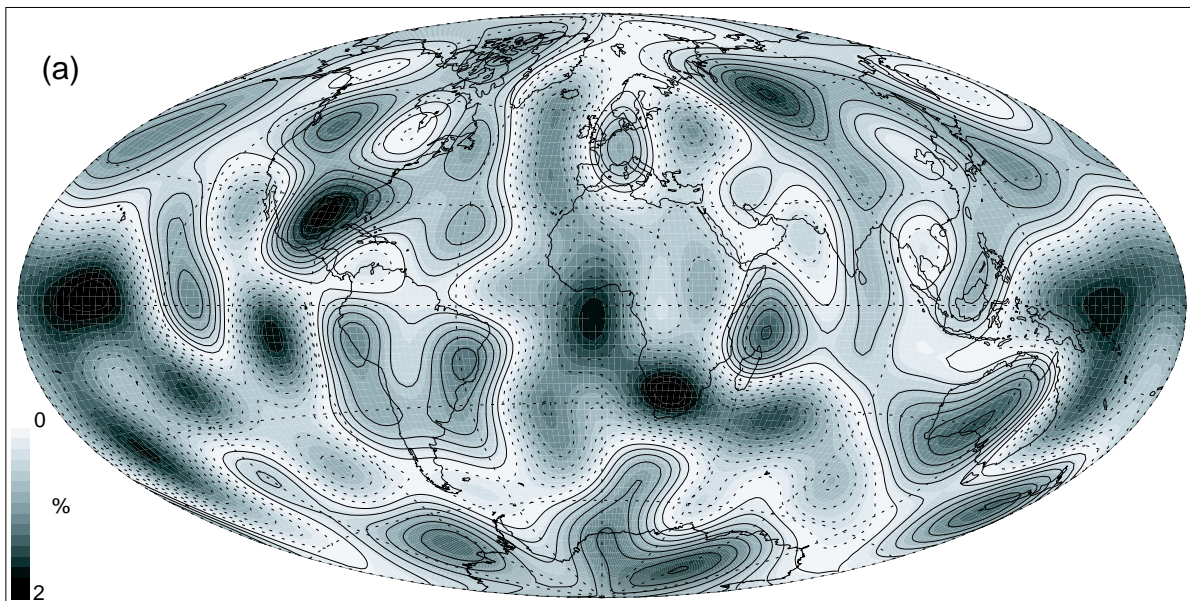
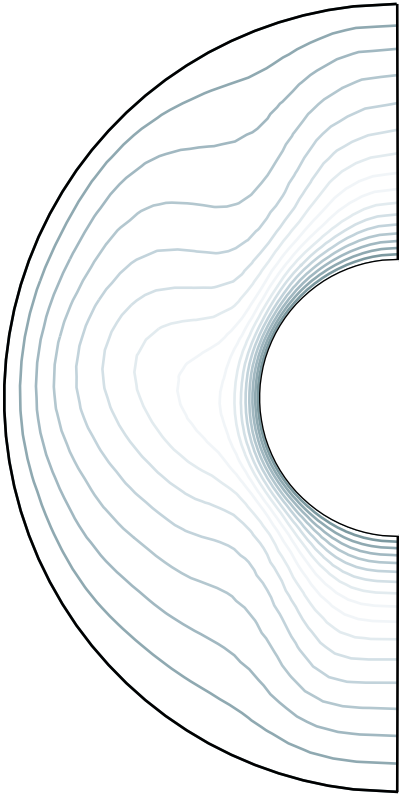
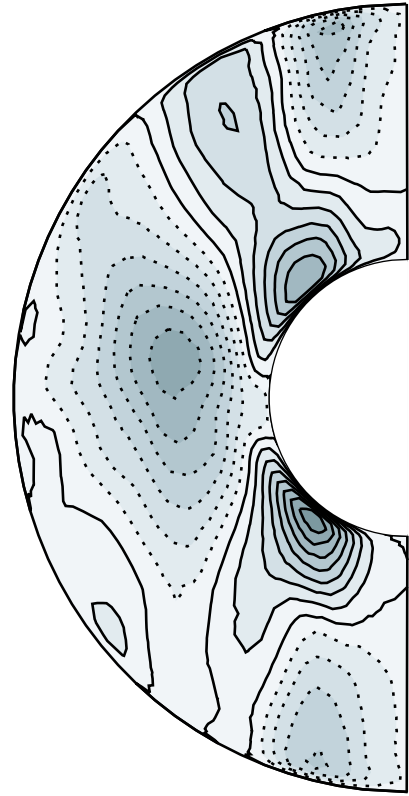


Fig. 5

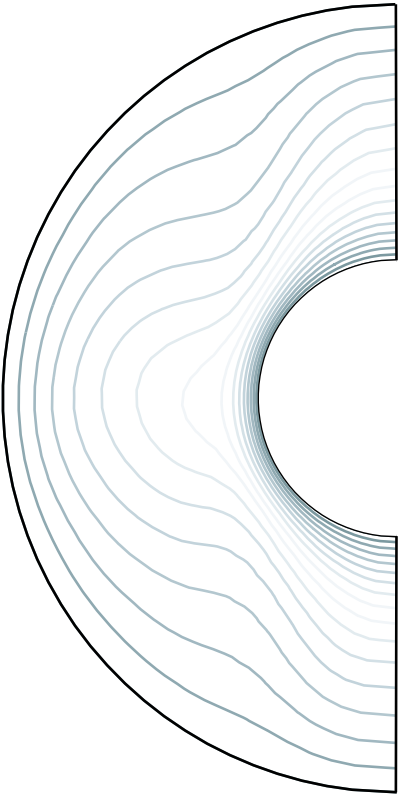
(a)



(b)



(c)



(d)

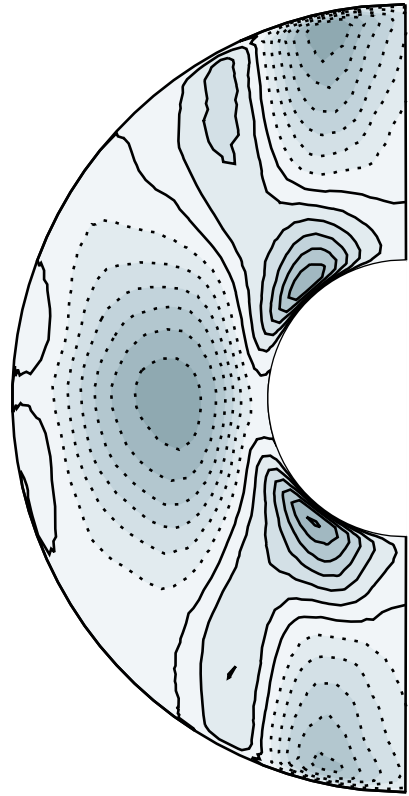


Fig. 6

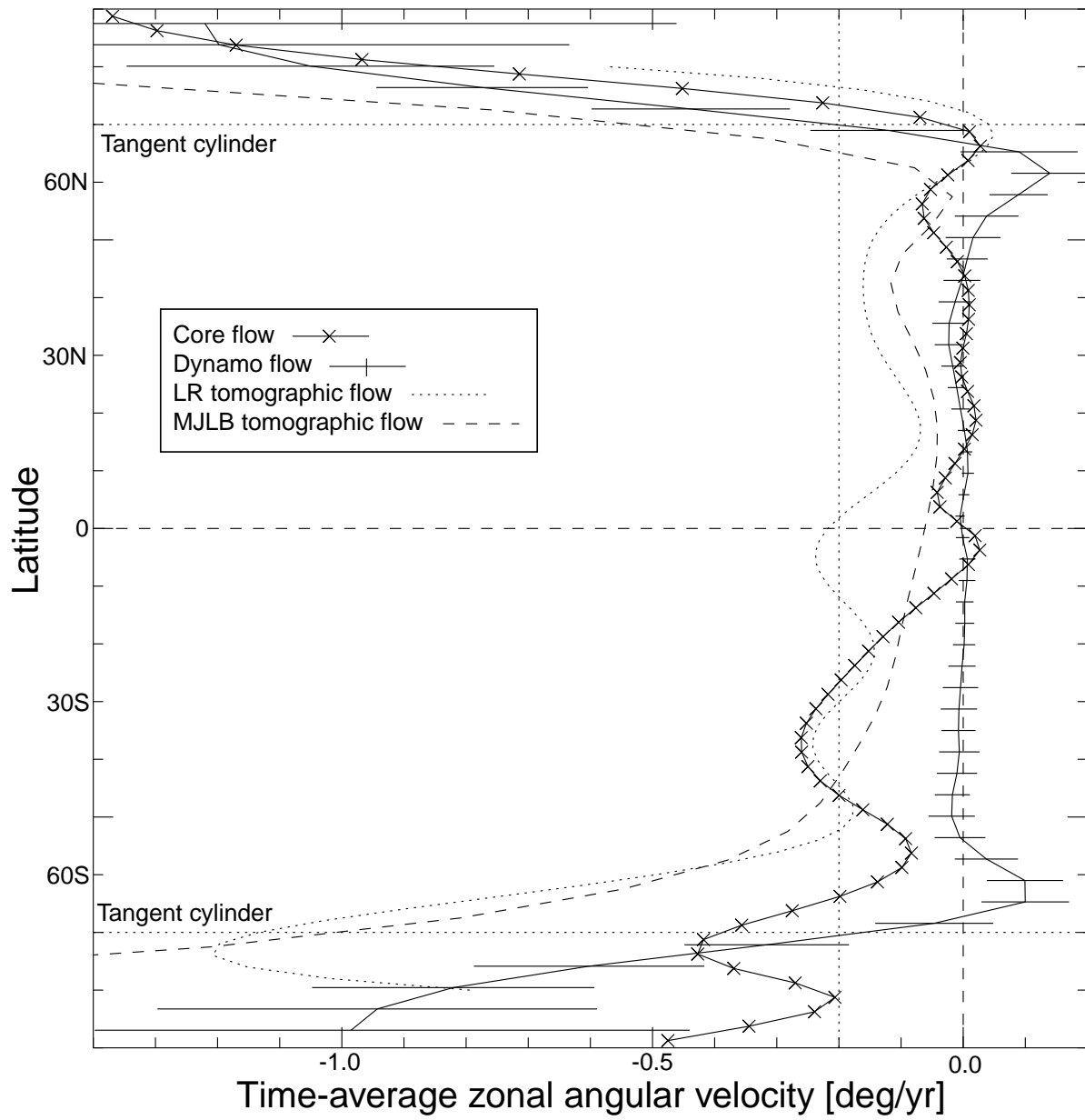


Fig. 7

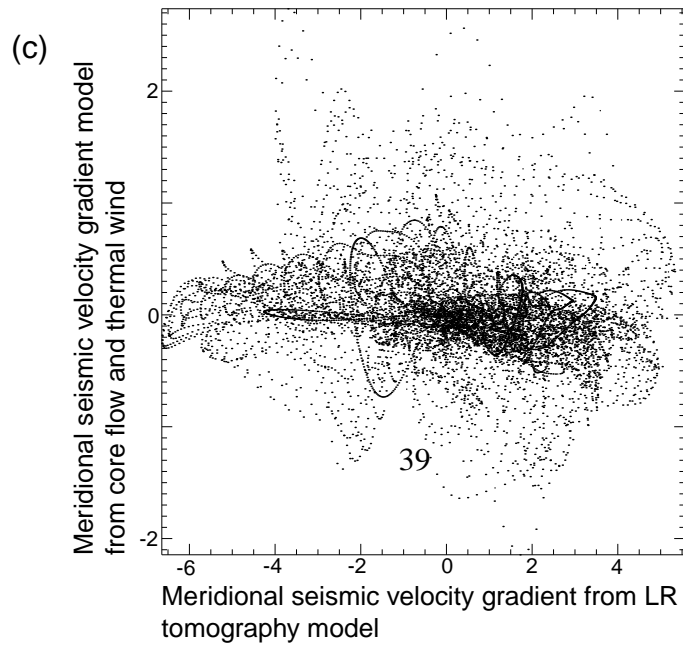
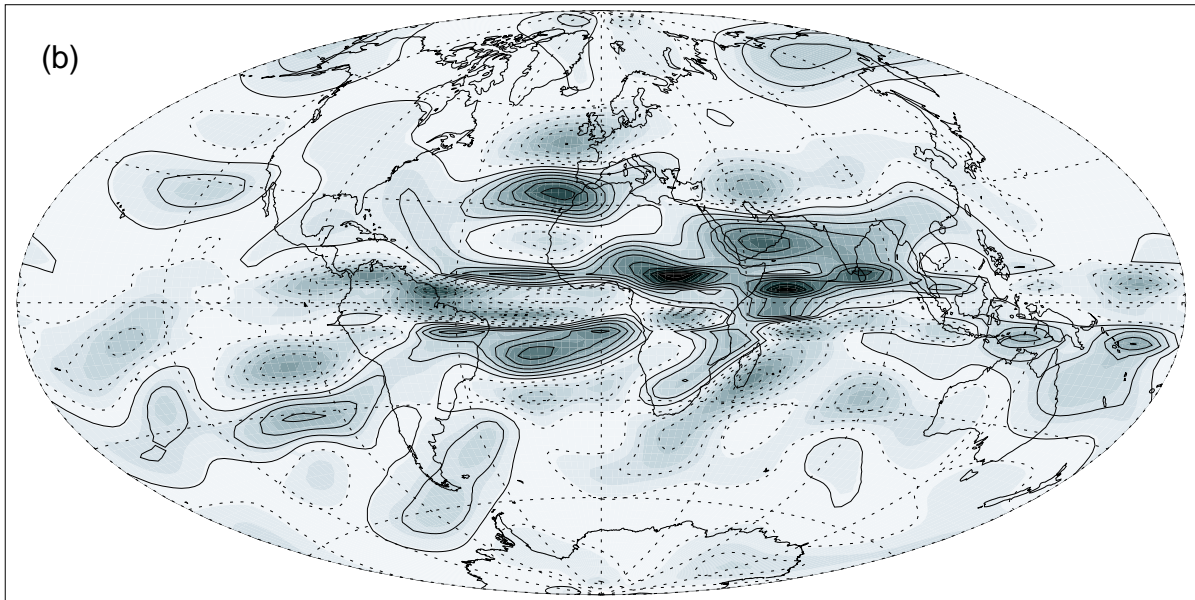
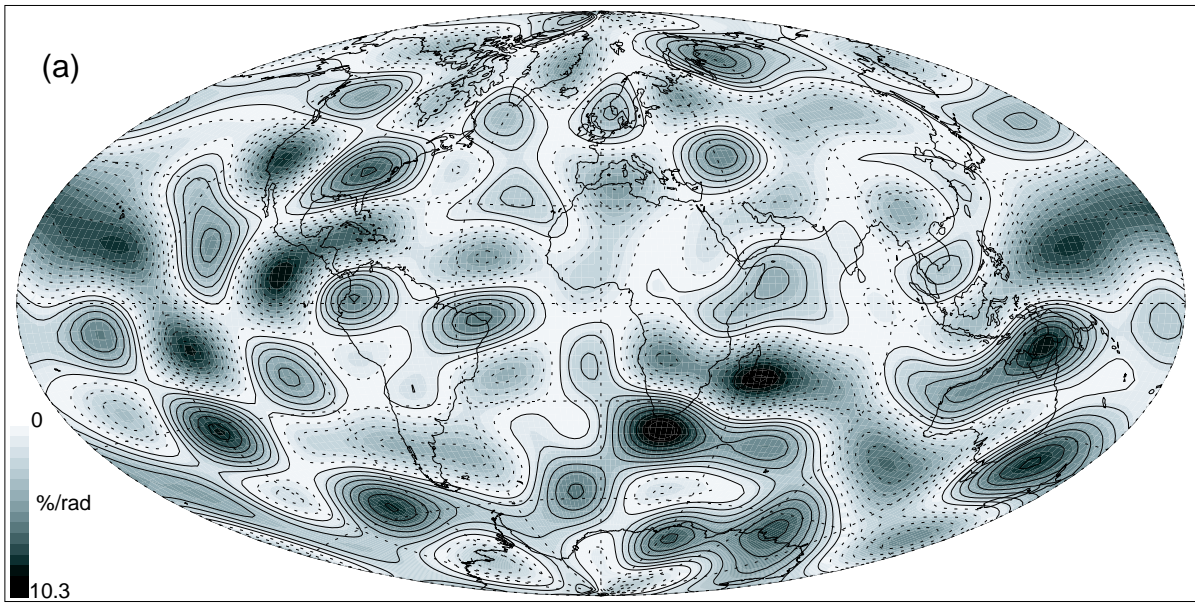


Fig. 8

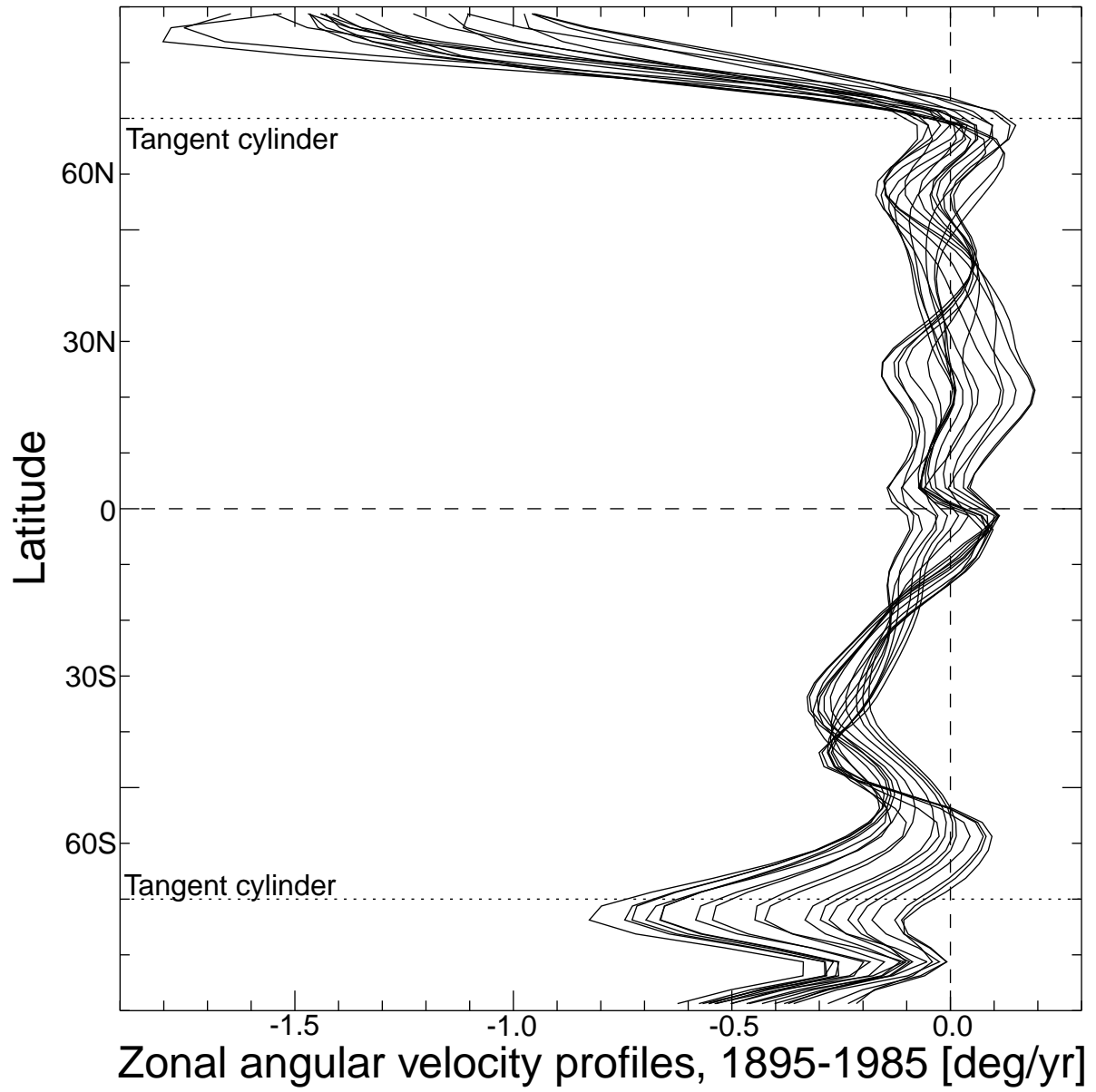


Fig. 9

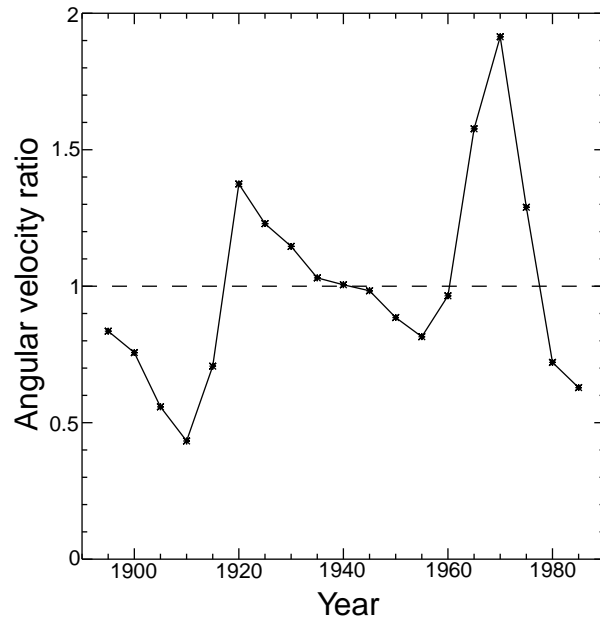


Fig. 10

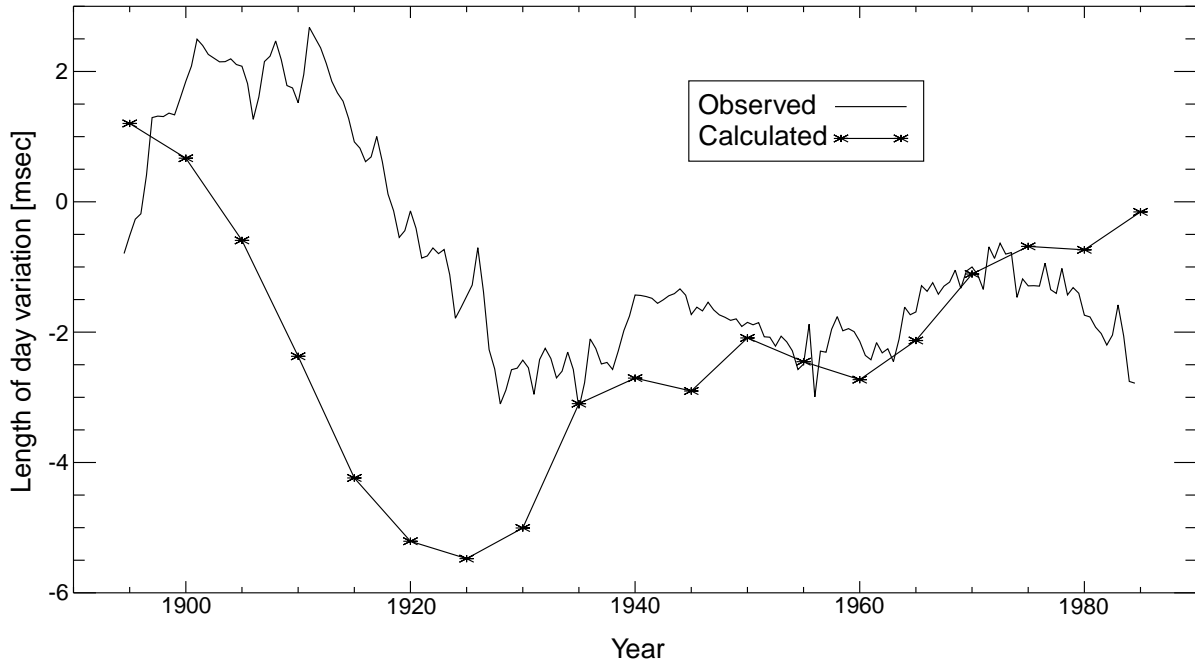


Fig. 11

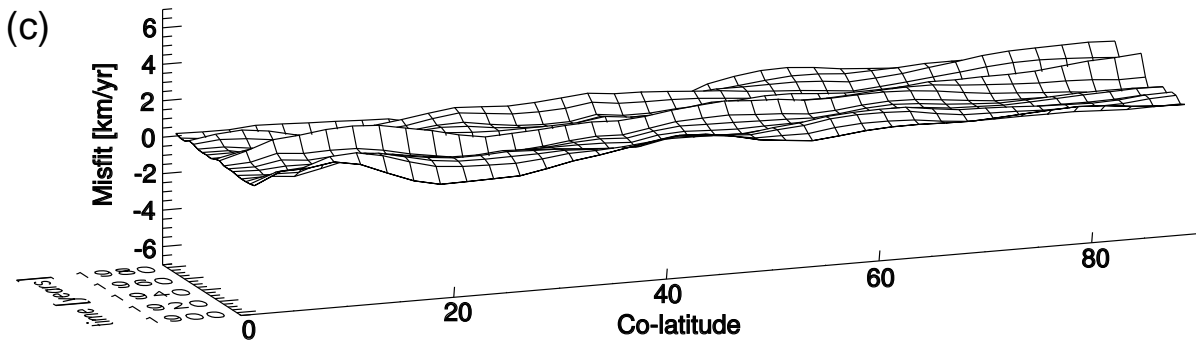
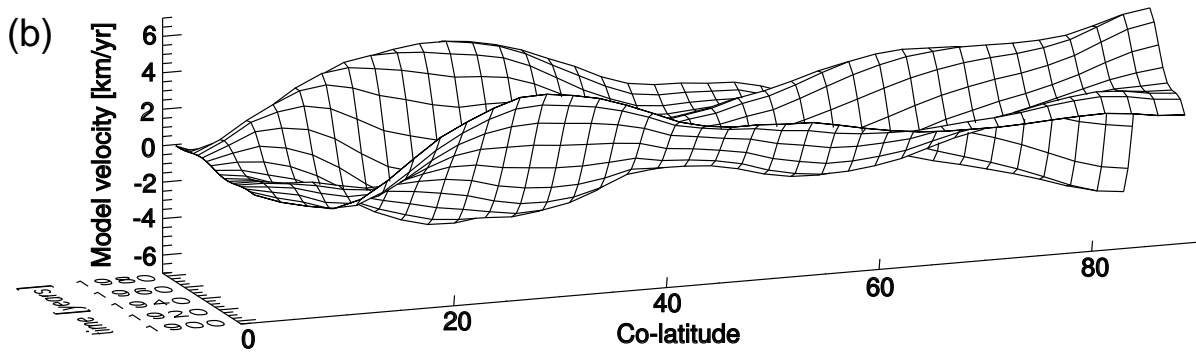
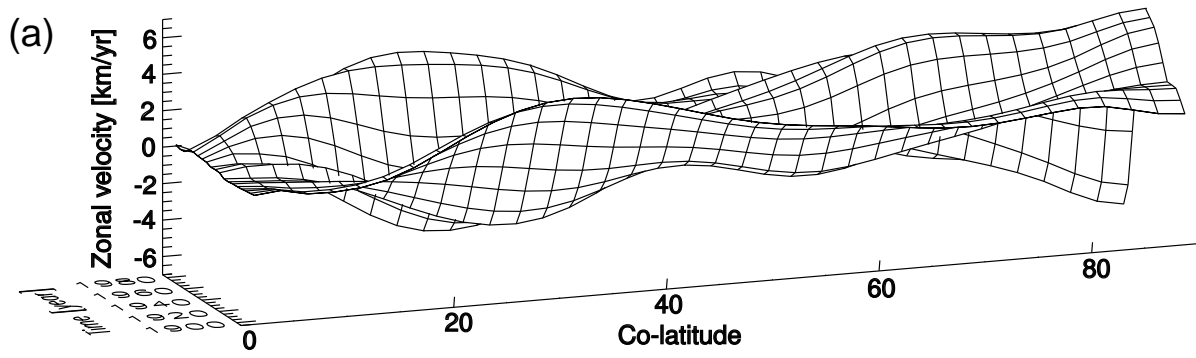


Fig. 12

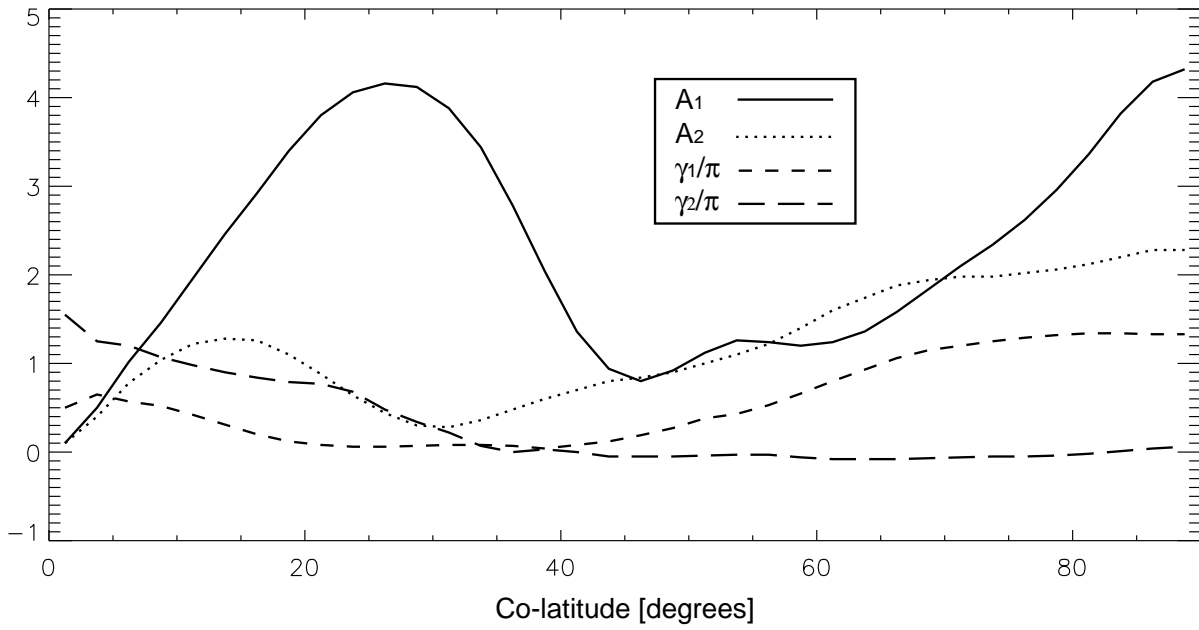


Fig. 13